

# 1 **Insights into *in vivo* adipocyte differentiation through cell-** 2 **specific labeling in zebrafish**

3  
4 Running title: *In vivo* adipocyte differentiation

5  
6 **Paola Lepanto (1)\*#, Florencia Levin (1)\*, Uriel Koziol (2), Leonel Malacrida (3,4),**  
7 **José L. Badano (1)#.**

8 (1) Human Molecular Genetics Lab, Institut Pasteur Montevideo, Uruguay

9 (2) Sección Biología Celular, Facultad de Ciencias, Universidad de la República,  
10 Montevideo, Uruguay

11 (3) Advanced Bioimaging Unit, Institut Pasteur Montevideo and Universidad de la  
12 República, Montevideo, Uruguay

13 (4) Departamento de Fisiopatología, Hospital de Clínicas, Facultad de Medicina,  
14 Universidad de la República, Montevideo, Uruguay

15 \*shared first authorship

16 #To whom correspondence should be addressed: José L. Badano

17 jbadano@pasteur.edu.uy, Paola Lepanto plepanto@pasteur.edu.uy, Institut Pasteur de  
18 Montevideo, Mataojo 2020, Montevideo CP11400, Uruguay; Tel: (598) 2 5220910.

19 Key words: zebrafish, adipocyte, Nile Red, blood vessels

## 20 21 **Summary statement**

22 Analysis of the differentiation of adipocytes *in vivo* through cell-specific labeling in  
23 zebrafish, revealed their early interaction with blood vessels as well as early lipid  
24 metabolic changes.

25 **Abstract**

26 White adipose tissue hyperplasia has been shown to be crucial for handling excess  
27 energy in healthy ways. Though adipogenesis mechanisms have been underscored *in*  
28 *vitro*, we lack information on how tissue and systemic factors influence the  
29 differentiation of new adipocytes. While this could be studied in zebrafish, adipocyte  
30 identification currently relies on neutral lipid labeling, thus precluding access to cells in  
31 early stages of differentiation. Here we report the generation and analysis of a  
32 zebrafish line with the transgene *fabp4(-2.7):EGFPcaax*. *In vivo* confocal microscopy of  
33 the pancreatic and abdominal visceral depots of transgenic larvae, revealed the  
34 presence of labeled mature adipocytes as well as immature cells in earlier stages of  
35 differentiation. Through co-labeling for blood vessels, we observed a close interaction  
36 of differentiating adipocytes with endothelial cells through cell protrusions. Finally, we  
37 implemented hyperspectral imaging and spectral phasor analysis in Nile Red labeled  
38 transgenic larvae and revealed the lipid metabolic transition towards neutral lipid  
39 accumulation of differentiating adipocytes. Altogether our work presents the  
40 characterization of a novel adipocyte-specific label in zebrafish and uncovers  
41 previously unknown aspects of *in vivo* adipogenesis.

## 42 Introduction

43 White adipose tissue (WAT) is present in mammals as well as in the other vertebrates,  
44 in the form of anatomically and functionally distinct depots (Zwick et al., 2018). It is  
45 formed by adipocytes, adipocyte precursors and macrophages surrounded by a  
46 collagen-rich extracellular matrix, and is highly vascularized and innervated. In  
47 humans, both visceral and subcutaneous central WAT depots primarily play energy  
48 storage and endocrine functions, which are of central importance in the regulation of  
49 energy homeostasis. Thus, WAT dysfunction, which is usually associated with obesity,  
50 contributes to the development of metabolic syndrome associated-diseases such as  
51 type II diabetes, dyslipidemia and non-alcoholic fatty liver disease (Longo et al., 2019).  
52 Meanwhile, other depots such as those in the dermis, bone marrow and mammary  
53 gland, contribute to regulation of local innate immunity and to the repair of adjacent  
54 tissues (Zwick et al., 2018).

55 In humans, the localization and mode of remodeling of adipose tissue have been  
56 associated with healthy or pathological phenotypes (Hepler and Gupta, 2017).  
57 Macroscopically, the expansion of subcutaneous WAT (SAT) is considered healthier  
58 than the growth of visceral WAT (VAT), as well as its localization in peripheral  
59 (extremities) vs central (abdomen in men; abdomen and hips in women) depots. Also,  
60 the accumulation of fat can occur in previously existing mature adipocytes  
61 (hypertrophy) or in newly differentiated cells (hyperplasia). Importantly, different lines of  
62 evidence support an association between adipose tissue hyperplasia with a healthier  
63 state as compared to hypertrophy (Vishvanath and Gupta, 2019). Adipogenesis is the  
64 process whereby stem cell-like precursors become committed, generating pre-  
65 adipocytes which then differentiate into mature adipocytes. While initial formation of  
66 adipogenic progenitors occur in hematopoietic tissues (Hudak et al., 2014), adult  
67 progenitors reside locally associated to blood vessels of adipose tissue (Hilgendorf et  
68 al., 2019; Tang et al., 2008). Tissue environment and cellular composition may  
69 influence the differentiation of these locally residing progenitors (for example, (Schwalie  
70 et al., 2018)). Thus, the study of adipogenesis and its relationship with other elements  
71 in the tissue *in vivo*, is critical to understand normal and pathological processes.

72 Work on cultured cells has provided key information about transcriptional regulation of  
73 adipogenesis (Bahmad et al., 2020). Meanwhile studies in mice have been conducted  
74 to analyze the developmental origin of adipocyte progenitors (Hepler and Gupta, 2017).  
75 More recently, the use of zebrafish to analyze adipose tissue biology has captured  
76 attention as it promises to enable the study of the tissue and its cellular biology *in vivo*.

77 Zebrafish develops only white adipose tissue, which first appears in visceral depots in  
78 early larval stages (Flynn et al., 2009; Minchin and Rawls, 2017b). In contrast, mice  
79 develop first SAT depots in embryonic stages while VAT appears postnatally (Hudak et  
80 al., 2014). Importantly however, zebrafish adipocytes show the same subcellular  
81 characteristics, gene expression patterns and final distribution (visceral and  
82 subcutaneous) as in mammals (Flynn et al., 2009). Moreover, it has been reported that  
83 factors affecting body fat distributions in humans have comparable effects in zebrafish  
84 (Loh et al., 2020; Minchin et al., 2015). Thus, taking advantage of its fast external  
85 development and optical transparency, zebrafish is an ideal system to study cellular  
86 and tisular aspects of WAT development.

87 Current methods to label adipose tissue *in vivo* rely on the use of lipophilic dyes such  
88 as LipidTOX or Nile Red (Minchin and Rawls, 2017a). Nile Red is particularly useful  
89 because its absorption and emission spectral characteristics are modified according to  
90 the polarity of the environment surrounding the probe (Greenspan and Fowler, 1985).  
91 The emission of Nile Red in the context of neutral lipids is blue-shifted in comparison to  
92 when it is in the presence of polar lipids. This spectroscopic characteristic has been  
93 extensively used to label lipid droplets and to estimate the amount of adipose tissue in  
94 live larvae as well as to classify depots (Minchin and Rawls, 2017b). However, Nile  
95 Red stains all cell membranes, including the endoplasmic reticulum in which  
96 biogenesis of lipid droplets takes place (Olzmann and Carvalho, 2019). Lipid stores are  
97 composed of neutral lipids such as triacylglycerols and sterol esters, while polar lipids  
98 are present during droplet formation as well as during lipolysis. Maulucci et al.  
99 developed an approach to generate a lipid metabolic index using hyperspectral imaging  
100 of Nile Red and spectral phasor analysis (Di Giacinto et al., 2018; Maulucci et al.,  
101 2018). Thus, this method allowed them to differentiate among cells forced to carry out  
102 lipid movement (lipid storage or lipolysis) and those in a resting state. The application  
103 of this method to live larvae as well as the study of the interaction of adipocytes with  
104 other cells in the tissue would require to specifically label adipocytes independently of  
105 their fat load.

106 To address this we decided to generate an adipocyte specific reporter zebrafish line.  
107 Up to date, no factor has been identified that is expressed in all fat depots in mice  
108 (Cleal et al., 2017). However, there are several genes that are upregulated in  
109 adipocytes in different stages during differentiation, like those used extensively in cell  
110 culture of mammalian cells to monitor differentiation progress (Tang and Lane, 2012).  
111 As expected, much less information is available from zebrafish. We therefore selected  
112 early and late genes which are commonly used as adipocyte differentiation markers in

113 mammalian cell culture models and with previous evidence of being expressed in  
114 zebrafish adipose tissue (Imrie and Sadler, 2010), cloned their putative promoter  
115 regions and generated transgenesis constructs. We show here that a *fabp4a* -2,7kb  
116 proximal genomic region effectively drives the expression of EGFP in adipocytes both  
117 previous to and during the accumulation of fat. Membrane tagging of GFP allowed us  
118 to observe the early interaction of adipocytes with blood vessels through adipocyte  
119 membrane protrusions. Furthermore, we adapted the method of Maulucci et al. by  
120 incorporating a three-component analysis in the phasor plot, which enabled us to  
121 analyze the lipid metabolism of EGFP-positive cells in live larvae before the formation  
122 of lipid droplets. Thus, this new zebrafish transgenic line is a valuable tool which will  
123 open new possibilities to study adipocytes and adipose tissue biology *in vivo*.

## 124 Results

### 125 ***fabp4a(-2.7):EGFPcaax transgene is expressed in early and mature adipocytes.***

126 Based on previously reported data on cell culture models and expression patterns in  
127 zebrafish we selected four different genes to work with: *adipoqb*, *cebpa*, *cfb*, *fabp4a*. All  
128 of them were previously reported to be expressed in zebrafish adipose tissue in larvae  
129 and/or adults (Imrie and Sadler, 2010). Taking into account our analysis of the  
130 promoter regions, we cloned approximately 2 kb of the proximal part of the promoter for  
131 each gene (see Materials and methods), and generated transgenesis constructs using  
132 the Tol2 system bearing the cardiac light chain myosin reporter gene, *cmlc2:GFP*, as  
133 an early selection marker (Fig. 1A). These constructs were injected together with  
134 mRNA coding for Tol2 transposase in the cytoplasm of one-cell stage embryos.  
135 Twenty-four hours post-fertilization (hpf) embryos with GFP expressing-cells in their  
136 hearts were selected for further breeding. We then analyzed larvae of 15-21 days post-  
137 fertilization (dpf) in the stereomicroscope, observing the presence of labelled cells for  
138 the constructions with *cebpa* and *fabp4a* promoters. However, only in the latter case  
139 the EGFPcaax signal coincided with lipid droplets in mature adipocytes recognizable  
140 through transmitted light. Moreover, only in the case of larvae injected with the *fabp4a(-*  
141 *2.7):EGFPcaax* construct we observed mature adipocytes labelled along several  
142 generations (Fig. 1B). Therefore, we decided to continue working only with the *fabp4a(-*  
143 *2.7):EGFPcaax* line.

144 First, to assess EGFP expression in live *fabp4a(-2.7):EGFPcaax* larvae we stained  
145 individuals of different stages with the lipophilic dye LipidTOX-Red and analyzed them  
146 using epifluorescence microscopy. We observed EGFPcaax signal in the surface of  
147 mature adipocytes, both in the pancreatic and abdominal depots (PVAT and AVAT  
148 respectively) (Fig. 1B, asterisks). Of note, expression levels varied among cells and  
149 this effect remained even after several outcrosses with the wild type fish line. We also  
150 analyzed other early-forming depots (renal, ocular and subcutaneous in fins) but failed  
151 to detect cells with expression of EGFP. Interestingly, both in PVAT and AVAT, besides  
152 mature adipocytes with readily visible lipid droplets, we observed EGFPcaax-positive  
153 (EGFP+) cells that had smaller lipid accumulations as well as cells that had no  
154 detectable LipidTOX-Red signal (Fig. 1B, single and double arrows respectively).  
155 Based on the fact that mammalian *fabp4* is expressed during adipocyte differentiation  
156 (Tang and Lane, 2012), these results indicated that EGFP+ cells with no visible lipid  
157 droplets (to which we refer as EGFP+/LD- from now on) were likely adipocytes at initial  
158 stages of differentiation.

159

160 ***fabp4a(-2.7):EGFPcaax* transgene expression pattern recapitulates the adipose**  
161 ***tissue expression domain of endogenous *fabp4a****

162 Embryonic *fabp4a* expression has been reported to be restricted to the lens, midbrain  
163 and the blood vessels of the head and trunk in 48 hpf embryos (Liu et al., 2007).  
164 Meanwhile, 15 dpf larvae present *fabp4a* expression in trunk vessels and in early  
165 adipocytes (Flynn et al., 2009). To determine the expression pattern of the *fabp4a(-*  
166 *2.7):EGFPcaax* transgene, we analyzed several developmental stages and compared it  
167 with endogenous *fabp4a* expression. For this, endogenous *fabp4a* expression was  
168 assessed using fluorescent whole mount *in situ* hybridization (WMISH), and *fabp4a(-*  
169 *2.7):EGFPcaax* transgene expression through immunolabeling with an anti-GFP  
170 antibody.

171 First, we checked the specificities of WMISH probes using *fli1:EGFP* transgenic  
172 embryos, which express EGFP in blood vessels, useful as an anatomical reference.  
173 For that, 2 dpf wild type embryos were fixed and processed for WMISH as described in  
174 the “Materials and methods” section. As specificity controls, we used the *fabp4a* sense  
175 probe (negative control) and an antisense probe for *slit2* (additional specificity control).  
176 To detect EGFP, we performed a final immunolabeling step. We observed a clear  
177 signal corresponding to *fabp4a* transcripts when the WMISH was performed with the  
178 antisense probe, which co-localized with *fli1:EGFP* immunodetection almost completely  
179 (Fig. S1; note the presence of brain cells positive for *fabp4a* antisense probe without  
180 *fli1:EGFP* labeling). Neither of the other two probes generated similar patterns: no  
181 specific signal was observed with the *fabp4a* sense probe while the *slit2* antisense  
182 probe labeled the ventro-medial part of the neural tube as reported previously (Davison  
183 and Zolessi, 2020). These results corroborated the specificity of the *fabp4a* antisense  
184 probe and validated the post-WMISH immunofluorescence procedure and reagents.

185 To compare the distribution of transgenic *fabp4a(-2.7):EGFPcaax* expression with that  
186 of endogenous *fabp4a* in larvae, we performed WMISH in individuals of around 21 dpf,  
187 immunolabeled them with anti-GFP and analyzed them *in toto* using confocal  
188 microscopy. Endogenous expression was observed in the PVAT and AVAT areas with  
189 the *fabp4a* antisense probe, coinciding with cells expressing EGFP (Fig. 2A). The  
190 specific signal was not observed with the *fabp4a* sense probe (Fig. 2B). Also, EGFP  
191 expression was evidenced in pigment cells in live embryos (Fig. S2). This expression  
192 pattern was not described before for endogenous *fabp4a* and, in larvae processed for  
193 WMISH, expression of endogenous *fabp4a* was not observed in superficial pigment

194 cells (Fig. 2C, single arrows). Instead, we did observe staining for endogenous *fabp4a*  
195 in blood vessels (Fig. 2C, double arrows). In conclusion, the expression pattern of the  
196 transgene recapitulates the endogenous pattern of *fabp4a* in the adipose tissue, but  
197 not within blood vessels or in the brain.

198

### 199 ***Development of early adipocytes in vivo and their relationship with blood*** 200 ***vessels.***

201 Our results therefore supported the hypothesis that the *fabp4a(-2.7):EGFPcaax*  
202 transgene marks adipocytes during differentiation. To test this we analyzed live larvae  
203 and embryos of different stages using confocal microscopy. First, we analyzed  
204 embryos in search of early expression of *fabp4a(-2.7):EGFPcaax*. *In vivo* confocal  
205 analysis of 2 dpf and 5 dpf embryos showed expression of EGFP in cells along the  
206 antero-posterior axis at dorsal, lateral and ventral positions, all reminiscent of pigment  
207 cells (Fig. S2A and C, double arrows). The presence of early labeling of pigment cells  
208 suggested that this expression domain corresponded to ectopic expression of *fabp4a(-*  
209 *2.7):EGFPcaax* in the transgenic embryos. To discard autofluorescence or dispersion  
210 of light by pigments, we immunostained fixed embryos with anti-GFP antibody. We  
211 observed immunostaining co-localizing with EGFP fluorescence (Fig. S2B and D,  
212 double arrows), thus confirming that in our fish line pigment cells are labeled by  
213 *fabp4a(-2.7):EGFPcaax*.

214 Previously, it has been reported that lipid droplets are first evident at the right side of  
215 the abdomen of early larvae, in ventral and posterior position with respect to the swim  
216 bladder (Flynn et al., 2009; Minchin and Rawls, 2017b). Thus we turned our attention  
217 into that region in larval stages and stained lipid droplets with LipidTOX-Red.

218 Interestingly, early larvae of standard length (SL) 4.5 mm (8 dpf) show labeling of small  
219 cells within the abdomen. At higher magnification we observed the expected surface  
220 localization of EGFP. However, these cells did not present lipid droplets (Fig. 3A). We  
221 also observed labeling of cells within the trunk in dorsal positions which corresponded  
222 to the presence of pigment cells in transmitted light images. Other signals in the  
223 images corresponded to autofluorescence of gut contents in the ventral-most part of  
224 the larvae and light scattering of pigments in the dorsal half of the swim bladder (Fig.  
225 3A). Despite taking several actions to diminish these confounding signals (16 h food  
226 restriction previous to imaging; incubation with epinephrine), they were persistent.  
227 Nevertheless, based on the surface localization and intensity of the EGFP signal it was



228 possible to clearly distinguish these EGFP positive and lipid droplet-free cells  
229 (EGFP+/LD-).

230 Next, we evaluated older larvae to assess whether these EGFP+ cells in the abdominal  
231 region could accumulate lipids. Importantly, larvae of SL 5 and 6.3 mm (12 and 16 dpf  
232 respectively) clearly showed cells with surface EGFP signal and lipid droplets of  
233 various diameters (Fig. 3B and C). We also noted that some of these cells had irregular  
234 forms and projections (Fig. 3C, double arrows). Larvae of these ages also had rounder  
235 cells almost completely filled with one big lipid droplet (Fig. 3B and C). In mice, pre-  
236 adipocytes have been found to reside near blood vessels (Tang et al., 2008). Thus, we  
237 analyzed the relationship of early adipocytes with the vasculature by crossing *fabp4a(-*  
238 *2.7):EGFPcaax* fish with the *kd1r:mCherry* line, which labels endothelial cells. We  
239 observed EGFP+ cells both in close apposition and at some distance of vessels (Fig.  
240 4A). Moreover, when cells with lipid accumulation were observed in the PVAT or AVAT  
241 depots, some usually appeared in close contact with vessels, sometimes with  
242 extensions surrounding them (Fig. 4B).

243 We expanded our analysis until 21 dpf larvae (larvae of SL 7-8mm) and observed  
244 EGFP+ positive cells with different morphologies (Fig. 5A and B). We observed  
245 rounded cells filled with a single lipid droplet which likely correspond to mature  
246 adipocytes, in some cases having cell projections. Other cells, usually located at the  
247 periphery of the depots, typically showed one or more smaller lipid droplets and more  
248 irregular morphologies, also with membrane projections (Fig. 5A). In many occasions  
249 we observed cells in close proximity to vessels or with extensions surrounding them  
250 (Fig. 5B). Remarkably, in all stages analyzed in this work, EGFP+/LD- cells were  
251 present. These cells could be observed not only in the abdominal region in AVAT and  
252 PVAT but also surrounding the gut in different positions (Fig. 3B), including in the  
253 cloaca region (Fig. S3). Interestingly, using transmitted light and high magnification we  
254 observed inclusions within EGFP+/LD- cells (Fig. 5C). We performed time lapse  
255 acquisitions of those cells for a short period of time. During these time lapse movies we  
256 observed that inclusions moved within the cytoplasm (Movie 1). Furthermore, we  
257 observed that cells could remain static or have directional movement over a cell  
258 diameter distance (Movie 1). This behavior was accompanied by the formation of  
259 protrusions which were evident also in our single time point observations (Fig. 3B and  
260 5C).

261 Altogether, our results show that *fabp4a(-2.7):EGFPcaax* expressing cells are present  
262 in different larval stages, from just before the beginning of the accumulation of fat to

263 later stages where lipid depots are readily visible. Furthermore, we found labeled cells  
264 with lipid droplets of different sizes, confirming that cells expressing *fabp4a(-*  
265 *2.7):EGFPcaax* in the abdominal region of larvae are adipocytes in different stages of  
266 differentiation. Even though our fish line also expresses EGFP in pigment cells, *in vivo*  
267 3D analysis of the abdominal region efficiently allowed us to distinguish early and  
268 mature adipocytes based on localization and cell shape. Furthermore, the results  
269 underscore a tight relationship between adipocytes and vessels during their  
270 differentiation, and the coexistence of EGFP+ lipid-filled cells with EGFP+/LD- cells in  
271 the tissue.

272

273 ***Analysis of the lipid metabolic profile of early adipocytes with Nile Red***  
274 ***fluorescence and spectral phasor plot analysis.***

275 As mentioned before, we hypothesized that EGFP+/LD- cells were in fact early  
276 adipocytes. Early adipocytes initiate lipid accumulation as part of its differentiation  
277 program, and thus would show a mixed lipid environment with neutral and polar  
278 components. The quantification of these components has been carried out before in  
279 cultured cells through Nile Red fluorescence analysis using spectral phasors (Di  
280 Giacinto et al., 2018; Maulucci et al., 2018). In our transgenic larvae, the fluorescence  
281 of EGFP could be used as a third component to identify the cells of interest (EGFP+  
282 cells). Thus, we took advantage of the spectral phasor analysis to study the Nile Red  
283 spectral shift in the presence of EGFP fluorescence. A similar approach has been used  
284 to study membrane polarity using LAURDAN in the presence of mRuby fluorescence  
285 (Sameni et al., 2018). For the cellular lipid metabolic profile, wild type larvae stained  
286 with Nile Red or *fabp4a(-2.7):EGFPcaax* larvae with or without staining with Nile Red  
287 were imaged using hyperspectral detection and the images were analyzed using the  
288 advantages of the model-free spectral phasors approach (Fig. S4, the analysis  
289 procedure is described in depth in the “Material and methods” section) (Malacrida et  
290 al., 2017).

291 Wild type larvae stained with Nile Red or *fabp4a(-2.7):EGFPcaax* larvae without  
292 staining were analyzed first to set the extremes of the distributions in the phasor plot  
293 (Fig. S4B). Notice that the Nile Red fluorescence was spread in a trajectory due to the  
294 heterogeneity in the polarity of Nile Red environments provided by the intracellular  
295 membranes. The position along the trajectory represents pixels with different fractions  
296 of membranes with more or less polarity. In the EGFP+ cells labeled with Nile Red, the  
297 linear combination for the Nile Red was dragged toward the EGFP position (Fig. S4C).

298 Thus, the extremes of the Nile Red trajectory can be considered as two components  
299 and the EGFP as the third component. This strategy enabled us to generate masks for  
300 individual EGFP+ cells and to analyze their lipid polarity profile, avoiding the Nile Red  
301 signal from other cells. An example image is shown in Fig. S4C. Two cells, one with  
302 lipid droplets (cell A) and another without them (cell B), generated clusters at the  
303 phasor plot with unequivocally different distribution profiles. To analyze the lipid polarity  
304 profile on each of them, we obtained the polarity fractional plot (Fig. S4D). The analysis  
305 of cell A yielded a multimodal distribution with higher representation of intermediate  
306 zones, whereas cell B gave a single peak in the polar lipid region.

307 Using this approach, we analyzed EGFP+ cells in larvae at different stages.  
308 Representative examples of the observed profiles are shown in Fig. 6A and B.  
309 Seemingly mature adipocytes with a big lipid droplet showed a peak in Nile Red profile  
310 in regions corresponding to the accumulation of neutral lipids as expected (Fig. 6A and  
311 B, “cell D”). Interestingly, it was possible to observe a small peak towards longer  
312 wavelengths, representing polar lipid components in the same cells such as the plasma  
313 membrane. This was corroborated by the localization of these pixels: the former were  
314 localized centrally and the latter surrounded the whole cell (Fig. 6A, see Nile Red  
315 profile of “cell D”). EGFP+/LD- cells usually showed distributions enriched in polar  
316 components (Fig. 6A and B, “cell A”). Nevertheless, we imaged cells with several  
317 peaks or flatter distributions, probably representing transitions between polar and  
318 neutral lipid environments (Fig. 6A and B, “cell B” and “cell C”). To summarize and  
319 present all the profiles we observed, the center of mass (CM) and distribution range  
320 (RD) of the lipid polarity profiles, were calculated and used as characteristics of each  
321 distribution for comparison purposes (Materials and methods; Fig. S4D). Within the plot  
322 of center of mass vs distribution range (Fig. 6C) it is possible to separate a subgroup of  
323 cells with statistically distinct median (for the center of mass and distribution range) and  
324 variability (only for the center of mass) compared to those cells outside this region (Fig.  
325 6C and D, dashed line). The low CM and low DR means that the cells within this group  
326 are constituted mostly by polar lipids. These cells represent over 50% of the cells  
327 analyzed from 8 to 16 dpf (Fig. 6E). The rest of the cells analyzed lay outside the low  
328 CM-low DR region due to increasing accumulation of neutral lipids, which extend the  
329 DR and bias the CM towards higher values. The percentage of cells analyzed that can  
330 be classified in this sub-group increased with larvae age (Fig. 6E). Of note, we  
331 observed cells with distinct lipid polarity profiles among larvae of similar standard  
332 length and in some cases within the same larvae (Fig. 6E). These observations imply  
333 the coexistence of several stages of adipocyte differentiation within the same larvae

334 and suggest that differentiation *in vivo* is continuous and asynchronous. These results  
335 indicate that our zebrafish *fabp4a(-2.7):EGFPcaax* transgenic line together with  
336 hyperspectral imaging and the spectral phasor analysis shown here is a powerful tool  
337 to study changes of the intracellular lipid environment in differentiating adipocytes in  
338 live zebrafish larvae.

## 339 Discussion

340 A number of studies have started to address the role of compounds on lipid metabolism  
341 and storage using zebrafish as a model system (Landgraf et al., 2017). Current  
342 knowledge on zebrafish adipose tissue is restricted to fat accumulation capacity using  
343 lipophilic dyes due to the lack of specific cell markers. Here we generated and  
344 analyzed a new zebrafish line to specifically label adipocytes along their differentiation  
345 *in vivo*.

### 346 ***Expression pattern of fabp4a(-2.7):EGFPcaax***

347 We generated a new transgenic line cloning the proximal part of the promoter of the  
348 lipid transporter gene *fabp4a* and used it to direct the expression of a membrane form  
349 of EGFP. It was shown previously that *fabp4a* is expressed in the lens, midbrain as  
350 well as in blood vessels in the head and trunk of 2 dpf embryos (Liu et al., 2007), an  
351 expression pattern that we also observed with our WMISH assay in 2 dpf embryos.  
352 However, the *in vivo* analysis of 2 and 5 dpf embryos showed that *fabp4a(-*  
353 *2.7):EGFPcaax* transgene is not expressed in either blood vessels, midbrain or lens  
354 cells. In the case of 15 dpf larvae, *fabp4a* mRNA was previously reported to be  
355 expressed in abdominal cells with or without neutral lipid accumulation as well as in  
356 trunk vessels (Flynn et al., 2009). Our WMISH assay in larvae showed the expression  
357 of endogenous *fabp4a* in PVAT and AVAT depots, co-localizing in some cells with  
358 expression of *fabp4a(-2.7):EGFPcaax* transgene. Thus, the expression pattern of  
359 *fabp4a(-2.7):EGFPcaax* recapitulates primarily the adipose tissue domain of the  
360 endogenous expression pattern of *fabp4a*.

361 We also found that our *fabp4a(-2.7):EGFPcaax* transgene is expressed in surface  
362 pigment cells, a domain that does not coincide with the endogenous expression of  
363 *fabp4a*. One possible explanation for the lack of expression in some domains as  
364 mentioned earlier and the presence of an extra expression domain may be due to the  
365 lack of regulatory elements in the cloned region of the promoter. In that case, it would  
366 be possible to generate an improved fish line using BAC transgenesis. Alternatively,  
367 these extra domains of expression may be due to the action of enhancers present in  
368 the genomic region where the transgene was integrated. This is a common drawback  
369 of using random insertion of transposons for transgenesis and highlights the  
370 importance of using complementary strategies such as insulators or targeted transgene  
371 insertion (Caldovic et al., 1999; Roberts et al., 2014). Importantly however, this extra  
372 domain of expression did not hinder the utility of the transgenic line as it can be clearly

373 separated from the adipose-related signal by considering the relative position of cells in  
374 3D images.

375 Another particular aspect of this new transgenic fish line is that the level of expression  
376 of EGFP varies among cells. This variability remained even after three outcrosses with  
377 the wild type fish line, discarding a mosaicism-based effect. Thus, variation among  
378 cells may reflect different cellular states along differentiation which affect transcription  
379 from the cloned region of the *fabp4a* promoter, already known to be under a complex  
380 regulatory circuit. For example, binding sites for Ppar $\gamma$  and NF-K $\beta$  p50 which modulate  
381 transcription in reporter assays, have been reported in the promoter region used in our  
382 transgenic line (Laprairie et al., 2017). Moreover, Ppar $\gamma$  has been shown to bind the  
383 *fabp4* promoter in a brown adipocyte cell line (Tontonoz et al., 1994). Also, it has been  
384 reported that *fabp4* is regulated by VEGFA-DLL4/NOTCH and insulin-FOXO1  
385 pathways in endothelial HUVEC cells (Harjes et al., 2014). In humans, plasma levels of  
386 Fabp4, which is mainly produced by adipocytes, have been positively correlated with  
387 cardio-vascular disease, type-II diabetes and also with the progression of other  
388 diseases by a still undefined mechanism (Prentice et al., 2019). Thus, it would be  
389 interesting to analyze which factors contribute to the expression levels of *fabp4* as they  
390 may be of clinical relevance, and our results showing significant variability among  
391 adipocytes suggests this zebrafish line could be useful to this end.

### 392 ***Characterization of early adipocytes and their relationship to blood vessels***

393 As mentioned, our detailed microscopic analysis of *fabp4a(-2.7):EGFPcaax* larvae  
394 showed labelled cells with different characteristics. In the abdominal region, where  
395 WAT depots form, we observed both EGFP+ cells with lipid droplets of various sizes  
396 and others without them. These observations are in agreement with previous reports  
397 showing that *fabp4a* is expressed in cells with and without lipid droplets in early larvae  
398 (Flynn et al., 2009). Accordingly, EGFP+/LD- were present in early larvae (8-10 dpf)  
399 well before the initiation of fat accumulation. Notably, we also observed them in older  
400 larvae, coexisting with mature adipocytes in fat depots. Our analysis of Nile Red  
401 emission of EGFP+ cells/LD- revealed polar lipid or intermediate profiles. Thus, our  
402 results indicate that the *fabp4a(-2.7):EGFPcaax* transgene labels adipocytes ranging  
403 from early stages of differentiation to mature differentiated cells.

404 EGFP+/LD- cells presented inclusions when observed with transmitted light at high  
405 magnification. These inclusions were LipidTOX-negative and time lapse acquisitions  
406 showed that they were highly motile within the cell. Further experiments are required to  
407 determine the nature of these inclusions. One interesting possibility is that they may

408 represent initial stages of lipid droplet formation in which the amount of accumulated  
409 neutral lipids is not enough to be observed through LipidTOX labeling. LD are formed  
410 through accumulation of neutral lipids within the lipid bilayer of the ER, initially forming  
411 structures denominated lenses which grow and bud becoming lipid droplets (Olzmann  
412 and Carvalho, 2019). Genetic labeling tools that have been developed to evidence  
413 initial neutral lipid accumulations may be implemented to study the conservation of  
414 early lipid droplet formation mechanisms in zebrafish (Kassan et al., 2013; Wang et al.,  
415 2016).

416 WAT progenitors expressing PPAR $\gamma$  have been reported to reside in the mural  
417 compartment of adipose blood vessels in mice (Hilgendorf et al., 2019; Tang et al.,  
418 2008). As an analogy to mammals, some authors have hypothesized that WAT  
419 progenitors in zebrafish may derive from perivascular pre-adipocytes or, alternatively,  
420 from hematopoietic tissue located in the caudal region (Salmerón, 2018). In double  
421 labelled larvae, we found EGFP+/LD- cells both in contact and at a distance of blood  
422 vessels. In contrast, all EGFP+ cells with lipid droplets were observed in contact with  
423 blood vessels. EGFP+/LD- cells were also present surrounding the gut at different  
424 positions along the antero-posterior axis. Furthermore, our time lapse acquisitions  
425 revealed that these cells had the capacity to migrate. Thus, our results are consistent  
426 with the previous formulated hypothesis and *in vivo* time lapse microscopy of EGFP+  
427 cells combined with cell tracing may provide further information. For this, new methods  
428 to maintain larvae alive through extended periods of time will be needed, since in our  
429 hands, larvae remained alive only for a few hours after mounting in agarose.

430 Our work also provides information about adipocytes during differentiation and in their  
431 mature state. As our transgenic approach included a membrane associated form of  
432 EGFP, we could clearly identify the presence of membrane protrusions in early and  
433 mature adipocytes. In double-labelled larvae we could appreciate that these membrane  
434 protrusions reached blood vessels, suggesting the presence of physical connections.  
435 Whether this interaction is direct between cell membranes or indirect through another  
436 cell remains to be determined. Extensive evidence supports that several soluble factors  
437 coordinate adipogenesis and angiogenesis in obesity as well as in adipose-derived  
438 stem cell therapy (Hutchings et al., 2020; Lemoine et al., 2013). Furthermore, secretion  
439 of factors by peri-arterial adipocytes can mediate protection or inflammation of the  
440 adventitia and atherosclerosis development (Kim et al., 2020). Much less information is  
441 available on the interaction of adipocytes and vessels during formation of the adipose  
442 tissue (Cao, 2007). Our results suggest an intimate relationship of early adipocytes with  
443 blood vessels, probably through cell surface molecules. We hypothesize that these

444 interactions may be instrumental in acquisition of lipids from blood vessels as well as in  
445 regulation of growth of the adipose depot.

#### 446 ***Nile Red and phasor approach to characterize in vivo cell lipid metabolism***

447 We used the new *fabp4a(-2.7):EGFPcaax* line to implement a tool for *in vivo* analysis  
448 of lipid environment using Nile Red hyperspectral imaging and its analysis through  
449 spectral phasor plots (Maulucci et al., 2018). Early adipocytes initiate lipid accumulation  
450 as part of their differentiation program, and thus would show a mixed lipid environment  
451 with neutral and polar components in their profile. Indeed, as mentioned before,  
452 EGFP+/LD- cells showed different profiles, ranging from polar-lipid environment to  
453 intermediate polarity-lipid environment. Several groups have studied the lipid  
454 composition of *in vitro* differentiating adipocytes of different origins through disruptive  
455 methods (Miehle et al., 2020). For example, human undifferentiated adipocytes were  
456 enriched in membrane phospholipids such as phosphatidylethanolamines,  
457 phosphatidylcholines and sphingomyelins. Meanwhile completely differentiated cells  
458 were shown to present diacylglycerols, lysophosphatidylethanolamines and  
459 triacylglycerols in addition to membrane phospholipids. Thus our results are consistent  
460 with previous analysis, and importantly, provide a base to build on the metabolic  
461 analysis of individual cells in their natural context.

462 Our data show that the technique is sensitive enough to detect lipid environment  
463 changes in a non-invasive way and for a specific cell identity, opening the possibility of  
464 using this tool to evaluate the progression of differentiation *in vivo* or the effect of drugs  
465 on lipid metabolism or genetic interventions. Future development of other fish lines  
466 using earlier molecular markers will improve the observation of cells in different stages.  
467 For example, work in mice have used *pref1* and *zfp423* to mark adipose tissue  
468 progenitors and pre-adipocytes (Gupta et al., 2010; Hudak et al., 2014). Both of these  
469 genes are present in zebrafish and may be useful to track the origin of the adipocyte  
470 lineage.

#### 471 ***Conclusions and perspectives***

472 In this work we introduced a new zebrafish line labeling adipocytes from early stages  
473 up to fully differentiated cells. Furthermore, we described the interaction of early and  
474 differentiated adipocytes with blood vessels and evidenced early lipid metabolic  
475 changes *in vivo*. We anticipate that the new transgenic line described here will be a  
476 useful tool to study the cell biology of adipocytes in the context of the tissue and the  
477 whole organism, their interaction with blood vessels and their differentiation *in vivo*.  
478 Adipogenesis is highly variable among depots in mammals (Hepler and Gupta, 2017),



479 thus it may be an advantage to use zebrafish for analysis of common conserved  
480 cellular mechanisms. Recently, new fish lines labeling lipid droplets have been  
481 generated (Lumaquin et al., 2020; Wilson et al., 2021) which may be combined with the  
482 *fabp4a(-2.7):EGFPcaax* line presented here for screening approaches focused on  
483 genetic and environmental factors affecting early adipocyte differentiation. The *fabp4a(-*  
484 *2.7):EGFPcaax* fish lines and the genetic tools available in zebrafish, combined with  
485 two-photon and multiplexing microscopy will surely provide a powerful platform to gain  
486 in depth information on adipogenesis and its *in vivo* determinants.

## 487 **Materials and methods**

### 488 ***Zebrafish maintenance, breeding and diets.***

489 We worked with TAB5 (wild type fish line), *kdlr:mCherry* (blood vessel labeling (Wang  
490 et al., 2010)) and *fli1:EGFP* (blood vessel labeling (Lawson and Weinstein, 2002)).  
491 *Danio rerio* adults were maintained in a stand-alone system (Tecniplast), at 28 °C, 800  
492 µS/cm<sup>2</sup>, and pH 7.5, with a diet based on live 48 hour-post eclosion *Artemia salina*  
493 (artemia cyst from Artemia International) and pellet (TetraMin, tropical flakes, Tetra).  
494 Embryos were raised in petri dishes with aquarium water at 28.5 °C (50 larvae per 10  
495 cm petri dish) and bleached at 24 hours post-fertilization. For growth of larvae we used  
496 Larval AP100-1 (<50 µm; Zeigler) from 5 to 30 dpf and Golden Pearl Reef & Larval Diet  
497 (100-200 µm; Brine Shrimp Direct) from 15 to 30 dpf. Dry food were administered twice  
498 per day plus one extra feed of live 24 hour-post hatching *Artemia salina*.

499 Embryonic staging was performed according to Kimmel (Kimmel et al., 1995) up to 5  
500 dpf and larvae staging (after 5 dpf) was done according to Parichy (Parichy et al.,  
501 2009). Standard length (SL) is the distance between the tip of the nose and the caudal  
502 peduncle, and it correlates linearly with the growth of adipose tissue as well as the  
503 development of other characteristics in larval zebrafish (Minchin and Rawls, 2017b). All  
504 protocols (n° 007-19, 009-19, 010-19, 011-19) were approved by the Institut Pasteur de  
505 Montevideo ethics committee for the use of animal models (CEUA) and performed by  
506 trained, certified staff.

### 507 ***Promoter cloning***

508 For identification of the potential promoter regions we combined manual analysis and a  
509 trial version of Gene2Promoter software (Genomatix). We then designed primers using  
510 the Primer-Blast tool from NCBI (Table 1). Candidate primers were blasted against the  
511 whole zebrafish genome using the BLAT tool from UCSC Genome Browser. Restriction  
512 sites were added at their 5`end to enable directional cloning (underlined in Table 1).

513 We used zebrafish high-molecular weight genomic DNA, extracted as previously  
514 described (Green and Sambrook, 2014) from 48 hpf TAB embryos. For *fabp4a*, the  
515 BAC DKEY-241P5 (Source BioScience) was used as a template. Each region was first  
516 cloned into pCRII plasmid using TOPO-TA Cloning Kit (Thermo). After sequencing,  
517 they were sub-cloned into p5`Entry-MCS plasmid from Tol2 Kit (Kwan et al., 2007)  
518 through digestion and ligation with T4 ligase (Thermo). We recombined each p5`Entry  
519 vector with pMiddle Entry vector coding for EGFPcaax (caax is a prenylation signal,  
520 directing EGFP to the plasma membrane), p3`Entry Vector with poly-A signal and the

521 pDestTol2-CG2 backbone (with cardiac myosin light chain promoter directing the  
522 expression of GFP, *cmlc2:GFP*, and tol2 sites for insertion into the genome).

523 **Table 1.** Primers used for amplification of the selected promoter regions, its position in  
524 relation to the transcription start site and the size of the amplification product. The  
525 underlined regions correspond to the restriction enzyme site.

gene	forward primer	reverse primer	cloned region referenced to transcription start site	size (bp)
<i>adipoqb</i>	ACGT <u>CTCGAGCC</u> CAGCT GTTCTTGTGTAATCC	ACGT <u>GGATCCT</u> CAAAG ATTCTATATTAGCACAA TCAA	-1892 to +114	2006
<i>cfb</i>	AGCT <u>GGTACCT</u> TCTGAAC CAGACAGGGAATAAAGT C	ACGT <u>GGATCC</u> GTGTGC TTTAGCCTCTTGCC	-1032 to +234	1266
<i>cebpa</i>	ACGT <u>GTCGACT</u> CCGCTC GGGTAAATAAAGA	ACGT <u>GGATCC</u> AGCAAC CTGTCGTGACTGTG	-1903 to +107	2010
<i>fabp4a</i>	ACGT <u>GTCGACG</u> TGGTGT TTTGCAGTGGATG	ACGT <u>GGATCCT</u> GCACA AATTCAGTCACGAAA	-2367 to +336	2703

526

### 527 ***Transgenic line generation***

528 TAB5 embryos at one cell stage were injected with 10-20 pg of the desired vector plus  
529 10-20 pg of Tol2 Transposase mRNA . We then selected 24 hpf embryos showing GFP  
530 fluorescence in the heart. We grew these embryos until 15-21 dpf when we analyzed  
531 the presence of fluorescence in adipose tissue. Selected individuals were outcrossed  
532 with the wild-type line until the third generation.

### 533 ***Fixation, permeabilization and immunolabeling***

534 To decrease pigmentation, embryos were treated with PTU 0.3 % starting at 8 hpf. For  
535 the same purpose larvae were anesthetized using tricaine 0.04 g/L, incubated in  
536 epinephrine 10 mg/mL plus tricaine 0.04 g/L, mounted in methylcellulose and observed  
537 using the stereomicroscope to select larvae expressing GFP. Fixation was carried out  
538 in 4 % PFA in PBS overnight at 4 °C.

539 Fixed embryos and larvae were permeabilized and immunolabeled following the  
540 protocol described by Inoue and Wittbrodt with minor modifications (Inoue and  
541 Wittbrodt, 2011). Briefly, all steps were carried out at room temperature with agitation  
542 unless stated otherwise. Fixed embryos and larvae were washed in PBS plus 1 %  
543 Triton X100 (PBST) (3 x 10 mins), dehydrated in a methanol series (50:50 and 100:0  
544 methanol:PBST) (1 x 10 min each) and incubated in 100 % methanol at -20 °C for 20

545 min. After rehydration in the same methanol series, we performed an antigen retrieval  
546 step with 150 mM Tris-HCl pH 9 (5 min at RT and 15 min at 70 °C). After a wash step  
547 in PBST (10 min) and two washes in distilled water (5 min each) we further  
548 permeabilized samples incubating them in 100 % acetone at -20 °C for 20 min. Finally  
549 we washed the samples in PBST several times (6 x 5 min each). For  
550 immunofluorescence on WMISH embryos and larvae we followed the same protocol  
551 without the acetone permeabilization step.

552 For immunolabeling all steps were performed with agitation. We incubated  
553 permeabilized embryos and larvae in the blocking buffer (10 % FBS plus 1 % BSA in  
554 PBST) for 1 h at RT. Primary and secondary antibodies were diluted in the incubation  
555 buffer (1 % FBS plus 1 % BSA in PBST). Antibody incubations were performed at 4 °C  
556 for 3 days, and washes at RT with PBST. The antibodies used in this work were: anti-  
557 GFP (Invitrogen, 1/500), anti-rabbit-633 (Invitrogen, 1/1000).

#### 558 **Fluorescent Whole-Mount *in situ* Hybridization (WMISH)**

559 We cloned a region of *fabp4a* previously used for probe generation (Flynn et al., 2009)  
560 using the following primers: fwd: GATCAAATCTCAATTTACAGCTGTTG; rv:  
561 TTCAAAGCACCATAAAGACTGATAAT and oligodT retro-transcribed cDNA as a  
562 template. The amplified region was ligated into pGEM T-easy vector (Thermo).  
563 Selected clones were checked through digestion and sequencing. The selected clone  
564 has the region 195 to 648 from *fabp4a* mRNA sequence, spanning the 3' half of the  
565 CDS and part of the 3'UTR, flanked by T7 and SP6 promoters in 5' and 3' respectively.  
566 To synthesize the probes we amplified the template using T7 and SP6 primers and  
567 afterwards generated digoxigenin (DIG) labeled probes by in vitro transcription with T7  
568 or SP6 polymerases, using Digoxigenin-11-UTP (Merck). As an additional specificity  
569 control we used a *slit2* antisense probe which has already been tested (generously  
570 provided by C. Davison (Davison and Zolessi, 2020).

571 The WMISH technique was performed as previously described (Koziol et al., 2014) with  
572 modifications following Flynn et al. and Elizondo et al. (Elizondo et al., 2005; Flynn et  
573 al., 2009). A detailed protocol is available upon request. Briefly, embryos and larvae  
574 were fixed in 4 % PFA prepared in PBS-DEPC water overnight at 4°C. PFA was then  
575 replaced twice with 100 % methanol and samples were stored at -20°C until used. After  
576 rehydration in an ethanol series, larvae were permeabilized with 15 ug/mL Proteinase  
577 K (Fermentas) in PBS-0.1 % Tween-20 (PBS-T) for 10 min (for embryos) or 30 min (for  
578 larvae) at room temperature. After a rinse with triethanolamine buffer (0.1 M, pH 8),  
579 they were treated twice with acetic anhydride (0.25% v/v for five minutes each),

580 washed with PBS-T, refixed with 4 % PFA in PBS-T for 20 min and washed extensively  
581 with PBS-T at room temperature. Pre-hybridization was performed overnight at 60°C in  
582 hybridization buffer (50 % formamide, 5X SSC, 1 mg/mL Torula RNA, 100 ug/mL  
583 heparin, 1x Denhardt's solution, 0.1 % Tween-20, 0.1 % CHAPS, DEPC treated water).  
584 DIG labelled probes were denatured at 80°C for 3 min and diluted to 0.2 ng/uL in the  
585 hybridization buffer. Hybridization was performed at 58°C for 2 days with agitation.  
586 Washing steps were done in hybridization buffer at 58°C with agitation, twice for 10 min  
587 each, then three times with 2X SSC plus 0.1 % Tween-20 at 58°C for 20 min each,  
588 three times with 0.2X SSC plus 0.1% Tween-20 at 58°C for 30 min each, and finally  
589 twice with maleic acid buffer (MAB) at room temperature for 15 min. Samples were  
590 then blocked overnight at 4°C in 1 % blocking reagent (Roche) plus 5 % sheep serum  
591 in MAB and incubated with anti-DIG conjugated to Peroxidase (1/50; Merck) in 1 %  
592 blocking reagent diluted in MAB for 3 days at 4°C. Washing steps were done in MAB  
593 (three washes of five minutes, followed by three washes of one hour). Fluorophore  
594 deposition was carried out with fluorescein-tyramide, prepared and developed as  
595 described by Hopman et al. (Hopman et al., 1998). After washes in PBS-T, samples  
596 were stored in 80% glycerol in PBS at -20°C until used.

### 597 ***In vivo labeling and imaging***

598 For *in vivo* lipid labeling, selected larvae were incubated in a 10 cm petri dish (when  
599 labeled in group) or 12-well plate (when labeled individually) containing the lipophilic  
600 dye diluted in system water. We incubated the larvae with LipidTox Red (Invitrogen,  
601 1/5000) for 1 h at 28 °C or Nile Red (Sigma, 0.78 µM for adipose area quantification  
602 and 0.078 µM for emission spectra analysis) for 1 h at 28°C. Labeled individuals were  
603 anesthetized and incubated in epinephrine as described above and mounted in 0.8 %  
604 low melting point agarose in a 3.5 mm glass bottom petri dish. After solidification, the  
605 sample was covered with tricaine 0.04 g/L in system water. To ensure viability during  
606 the observation period, a block of agarose covering the region of the gills and the lower  
607 jaw was removed using a needle.

608 *In vivo* images were acquired using epifluorescence or confocal microscopy. For  
609 epifluorescence we used an Olympus IX81 with 10x UPlan FLN 0.3 NA and 20x UPlan  
610 FLN 0.5 NA Olympus objectives. Confocal microscopy images were acquired with  
611 either a Zeiss LSM 800 or Zeiss LSM 880 with a 25x LD LCI Plan-Apochromat 0.8 NA  
612 Imm Corr DIC M27 (glycerol, oil, water, silicone) Zeiss objective. Hyperspectral imaging  
613 of Nile Red fluorescence was done using the lambda module in the Zeiss LSM 880 with  
614 the 25x objective, excitation the 488 Argon laser line was used and the spectra

615 acquisition involved 22 step with 10 nm bandwidth (from 493 nm to 713 nm) using a  
616 PMT-GaAsP detector.

### 617 **Image analysis**

618 Length and area measurements as well as brightness-contrast adjustments were done  
619 using Fiji software (Schindelin et al., 2012).

620 For Nile Red hyperspectral data analysis we used the spectra phasor approach using  
621 Globals for Images SimFCS 4 software (G-SOFT Inc, Champaign, IL-USA). This  
622 method transforms the spectral data in each pixel to the real and imaginary component  
623 of the Fourier transform, as described earlier by Malacrida et al. (Malacrida et al.,  
624 2016):

$$625 \quad G(\lambda) = \frac{\int_{\lambda_{min}}^{\lambda_{max}} I(\lambda) \cos\left(\frac{2\pi n (\lambda - \lambda_i)}{\lambda_{max} - \lambda_{min}}\right) d\lambda}{\int_{\lambda_{min}}^{\lambda_{max}} I(\lambda) d\lambda} \quad (1)$$

$$626 \quad S(\lambda) = \frac{\int_{\lambda_{min}}^{\lambda_{max}} I(\lambda) \sin\left(\frac{2\pi n (\lambda - \lambda_i)}{\lambda_{max} - \lambda_{min}}\right) d\lambda}{\int_{\lambda_{min}}^{\lambda_{max}} I(\lambda) d\lambda} \quad (2)$$

627  $I(\lambda)$  is the intensity at each step,  $n$  the harmonic number and  $\lambda_i$  is the initial wavelength.  
628 Each pixel in the image will be located at a single (G, S) position at the spectral phasor  
629 plot, yielding a cluster of points due to all pixels in an image. This transformation does  
630 not modify the original data and does not involve any fitting or any assumption of  
631 components. The position at the phasor depends on the spectrum maximum (phase  
632 angle,  $\Theta$ ) and the full width at half maximum (Modulation, M) (Fig. S4A), as:

$$633 \quad M = \sqrt{S^2 + G^2} \quad (3)$$

$$634 \quad \theta = \arctan (S/G) \quad (4)$$

635 While, red spectral shift implies increasing phase angle, the band narrowing moves the  
636 position toward the spectral phasor perimeter (modulation increases).

637 The spectral phasor plot enables the use of vector properties, such as the linear  
638 combination and the reciprocity principle. The linear combination allows the  
639 quantification of multiple components in a mixture as a sum fractions of single emitters.  
640 In our experiments, Nile Red presented complex photophysics that involved the  
641 emission from polar and neutral environments (membrane and lipid droplets,  
642 respectively). Furthermore, our phasor plots had an extra component from expression  
643 of EGFP. Using the three-component analysis developed by Ranjit and collaborators,  
644 we decomposed the fraction of Nile Red in the pixels with EGFP signal (Ranjit et al.,  
645 2019). We defined two individual cursor positions (two of the vertices) from the Nile

646 Red trajectory extremes using images from wild-type larvae labelled with Nile Red, and  
647 the third position using images of unlabeled *fabp4a(-2.7):EGFPcaax* larvae. The  
648 reciprocity principle enables to trace back a region of interest from the spectral phasor  
649 (imaginary space) to the original image (real space; the opposite, from a segmentation  
650 in the real image to the phasor plot, is also possible). Using this property, we  
651 segmented individual cells selecting the corresponding pixels in the phasor plot. Then,  
652 we obtained the fractional contributions for the Nile Red trajectory as explained in detail  
653 elsewhere (Ranjit et al., 2019). For comparison purposes between different treatments  
654 we used the center of mass (CM) for the Nile Red fraction histogram as a central  
655 tendency value and the range of the distribution as a dispersion value. The CM for the  
656 distribution of each cell Nile Red fraction was calculated as

$$657 \quad \sum b \cdot f(x) / \sum f(x) \quad (5)$$

658 with “*b*” being the percentage of pixels at the particular fraction “*f(x)*” of the component  
659 “*x*” (Malacrida and Gratton, 2018). The range of the distribution or distribution range  
660 (DR) was considered as the *f(x)* interval which contains 96% of the pixels. For its  
661 calculation we used the accumulated distribution for *f(x)* and determined the difference  
662 between the *f(x)* values corresponding to 2% and 98% of the accumulated distribution.

### 663 **Statistical analysis**

664 The statistical analysis was performed using PAST software (Hammer et al., 2001) or  
665 Real Statistics Resource Pack software (Release 7.6, Copyright (2013 – 2021),  
666 Charles Zaiontz, [www.real-statistics.com](http://www.real-statistics.com), accessed on March 2021). For group  
667 comparisons we analyzed normality using Shapiro-Wilk test and homogeneity of  
668 variances using Levene test. Non-normal and homoscedastic distributions were  
669 compared with non-parametric tests (Kruskal-Wallis or Mann-Whitney with Bonferroni  
670 correction) as indicated in each case. Non-normal and heteroscedastic samples were  
671 rank transformed (Conover and Iman, 1981) and compared using Welch test and  
672 Games-Howell post-hoc test. For the comparison of coefficient of variation we used the  
673 Fligner-Killeen test. The Reduced Major Axis (RMA) method was used for regression of  
674 bivariate data. For comparison of slopes we used the method explained in (Warton et  
675 al., 2006).

676 **Acknowledgements:** We thank Luisa Berná for her help defining the putative  
677 promoter regions of our genes of interest and Hugo Naya for his advice on statistical  
678 analysis. We also thank Gisell Gonzales for her invaluable support in the zebrafish  
679 laboratory as well as Magdalena Cardenas and Flavio Zolessi for the revision and  
680 helpful comments about the manuscript.

681 **Competing interests:** No competing interests declared.

682 **Funding:** This work was supported by: PEDECIBA and Sistema Nacional de  
683 Investigadores- ANII to P.L., U.K., L.M. and J.L.B.; FOCEM - Fondo para la  
684 Convergencia Estructural del Mercosur (COF 03/11). LM was supported by the Chan  
685 Zuckerberg Initiative.

686 **Data availability:** All the data generated in the study is presented in the manuscript.

687 **List of Symbols and Abbreviations:** hpf: hours post-fertilization; dpf: days post-  
688 fertilization; WMISH: whole mount in situ hybridization; PVAT: pancreatic visceral adipose  
689 tissue; AVAT: abdominal visceral adipose tissue; SL: standard length.



690 **References**

- 691 **Bahmad, H. F., Daouk, R., Azar, J., Sapudom, J., Teo, J. C. M., Abou-Kheir, W.**  
692 **and Al-Sayegh, M.** (2020). Modeling Adipogenesis: Current and Future Perspective.  
693 *Cells* **9**, 2326.
- 694 **Caldovic, L., Agalliu, D. and Hackett, P. B.** (1999). Position-independent expression  
695 of transgenes in zebrafish. *Transgenic Research* **8**, 321–334.
- 696 **Cao, Y.** (2007). Angiogenesis modulates adipogenesis and obesity. *J. Clin. Invest.* **117**,  
697 2362–2368.
- 698 **Cleal, L., Aldea, T. and Chau, Y.-Y.** (2017). Fifty shades of white: Understanding  
699 heterogeneity in white adipose stem cells. *Adipocyte* **6**, 205–216.
- 700 **Conover, W. J. and Iman, R. L.** (1981). Rank Transformations as a Bridge Between  
701 Parametric and Nonparametric Statistics. *The American Statistician* **35**, 124.
- 702 **Davison, C. and Zolessi, F. R.** (2020). *Slit2 is necessary for optic axon organization in*  
703 *the zebrafish ventral midline.*
- 704 **Di Giacinto, F., De Angelis, C., De Spirito, M. and Maulucci, G.** (2018). Quantitative  
705 imaging of membrane micropolarity in living cells and tissues by spectral phasors  
706 analysis. *MethodsX* **5**, 1399–1412.
- 707 **Elizondo, M. R., Arduini, B. L., Paulsen, J., MacDonald, E. L., Sabel, J. L., Henion,**  
708 **P. D., Cornell, R. A. and Parichy, D. M.** (2005). Defective Skeletogenesis with Kidney  
709 Stone Formation in Dwarf Zebrafish Mutant for *trpm7*. *Current Biology* **15**, 667–671.
- 710 **Flynn, E. J., Trent, C. M. and Rawls, J. F.** (2009). Ontogeny and nutritional control of  
711 adipogenesis in zebrafish (*Danio rerio*). *Journal of Lipid Research* **50**, 1641–1652.
- 712 **Green, M. and Sambrook, J.** (2014). *Molecular Cloning: A Laboratory Manual.*
- 713 **Greenspan, P. and Fowler, S. D.** (1985). Spectrofluorometric studies of the lipid  
714 probe, Nile red. *Journal of Lipid Research* **26**, 781–789.
- 715 **Gupta, R. K., Arany, Z., Seale, P., Mepani, R. J., Ye, L., Conroe, H. M., Roby, Y. A.,**  
716 **Kulaga, H., Reed, R. R. and Spiegelman, B. M.** (2010). Transcriptional Control of  
717 Preadipocyte Determination by Zfp423. *Nature* **464**, 619–623.
- 718 **Hammer, O., Harper, D. A. T. and Ryan, P. D.** (2001). PAST: Paleontological  
719 Statistics Software Package for Education and Data Analysis. *Palaeontologia*  
720 *Electronica* **4**, 9.

- 721 **Harjes, U., Bridges, E., McIntyre, A., Fielding, B. A. and Harris, A. L.** (2014). Fatty  
722 Acid-binding Protein 4, a Point of Convergence for Angiogenic and Metabolic Signaling  
723 Pathways in Endothelial Cells. *Journal of Biological Chemistry* **289**, 23168–23176.
- 724 **Hepler, C. and Gupta, R. K.** (2017). The expanding problem of adipose depot  
725 remodeling and postnatal adipocyte progenitor recruitment. *Molecular and Cellular*  
726 *Endocrinology* **445**, 95–108.
- 727 **Hilgendorf, K. I., Johnson, C. T., Mezger, A., Rice, S. L., Norris, A. M., Demeter, J.,**  
728 **Greenleaf, W. J., Reiter, J. F., Kopinke, D. and Jackson, P. K.** (2019). Omega-3  
729 Fatty Acids Activate Ciliary FFAR4 to Control Adipogenesis. *Cell* **179**, 1289-1305.e21.
- 730 **Hopman, A. H. N., Ramaekers, F. C. S. and Speel, E. J. M.** (1998). Rapid Synthesis  
731 of Biotin-, Digoxigenin-, Trinitrophenyl-, and Fluorochrome-labeled Tyramides and  
732 Their Application for In Situ Hybridization Using CARD Amplification. *J Histochem*  
733 *Cytochem.* **46**, 771–777.
- 734 **Hudak, C. S., Gulyaeva, O., Wang, Y., Park, S., Lee, L., Kang, C. and Sul, H. S.**  
735 (2014). Pref-1 Marks Very Early Mesenchymal Precursors Required for Adipose Tissue  
736 Development and Expansion. *Cell Reports* **8**, 678–687.
- 737 **Hutchings, G., Janowicz, K., Moncrieff, L., Dompe, C., Strauss, E., Kocherova, I.,**  
738 **Nawrocki, M. J., Kruszyna, Ł., Wąsiatycz, G., Antosik, P., et al.** (2020). The  
739 Proliferation and Differentiation of Adipose-Derived Stem Cells in Neovascularization  
740 and Angiogenesis. *IJMS* **21**, 3790.
- 741 **Imrie, D. and Sadler, K. C.** (2010). White adipose tissue development in zebrafish is  
742 regulated by both developmental time and fish size. *Dev. Dyn.* **239**, 3013–3023.
- 743 **Inoue, D. and Wittbrodt, J.** (2011). One for All—A Highly Efficient and Versatile  
744 Method for Fluorescent Immunostaining in Fish Embryos. *PLoS ONE* **6**, e19713.
- 745 **Kassan, A., Herms, A., Fernández-Vidal, A., Bosch, M., Schieber, N. L., Reddy, B.**  
746 **J. N., Fajardo, A., Gelabert-Baldrich, M., Tebar, F., Enrich, C., et al.** (2013). Acyl-  
747 CoA synthetase 3 promotes lipid droplet biogenesis in ER microdomains. *Journal of*  
748 *Cell Biology* **203**, 985–1001.
- 749 **Kim, H. W., Shi, H., Winkler, M. A., Lee, R. and Weintraub, N. L.** (2020).  
750 Perivascular Adipose Tissue and Vascular Perturbation/Atherosclerosis. *ATVB* **40**,  
751 2569–2576.

- 752 **Kimmel, C. B., Ballard, W. W., Kimmel, S. R., Ullmann, B. and Schilling, T. F.**  
753 (1995). Stages of embryonic development of the zebrafish. *Developmental Dynamics*  
754 **203**, 253–310.
- 755 **Koziol, U., Rauschendorfer, T., Rodríguez, L. Z., Krohne, G. and Brehm, K.** (2014).  
756 The unique stem cell system of the immortal larva of the human parasite *Echinococcus*  
757 *multilocularis*. *EvoDevo* **5**, 10–33.
- 758 **Kwan, K. M., Fujimoto, E., Grabher, C., Mangum, B. D., Hardy, M. E., Campbell, D.**  
759 **S., Parant, J. M., Yost, H. J., Kanki, J. P. and Chien, C.-B.** (2007). The Tol2kit: A  
760 multisite gateway-based construction kit for Tol2 transposon transgenesis constructs.  
761 *Developmental Dynamics* **236**, 3088–3099.
- 762 **Landgraf, K., Schuster, S., Meusel, A., Garten, A., Riemer, T., Schleinitz, D.,**  
763 **Kiess, W. and Körner, A.** (2017). Short-term overfeeding of zebrafish with normal or  
764 high-fat diet as a model for the development of metabolically healthy versus unhealthy  
765 obesity. *BMC Physiology* **17**, 4–14.
- 766 **Laprairie, R. B., Denovan-Wright, E. M. and Wright, J. M.** (2017). Differential  
767 regulation of the duplicated *fabp7*, *fabp10* and *fabp11* genes of zebrafish by  
768 peroxisome proliferator activated receptors. *Comparative Biochemistry and Physiology*  
769 *Part B: Biochemistry and Molecular Biology* **213**, 81–90.
- 770 **Lawson, N. D. and Weinstein, B. M.** (2002). In Vivo Imaging of Embryonic Vascular  
771 Development Using Transgenic Zebrafish. *Developmental Biology* **248**, 307–318.
- 772 **Lemoine, A. Y., Ledoux, S. and Larger, E.** (2013). Adipose tissue angiogenesis in  
773 obesity. *Thromb Haemost* **110**, 661–669.
- 774 **Liu, R.-Z., Saxena, V., Sharma, M. K., Thisse, C., Thisse, B., Denovan-Wright, E.**  
775 **M. and Wright, J. M.** (2007). The *fabp4* gene of zebrafish (*Danio rerio*) – genomic  
776 homology with the mammalian FABP4 and divergence from the zebrafish *fabp3* in  
777 developmental expression: *fabp4* gene in zebrafish. *FEBS Journal* **274**, 1621–1633.
- 778 **Loh, N. Y., Minchin, J. E. N., Pinnick, K. E., Verma, M., Todorčević, M., Denton, N.,**  
779 **Moustafa, J. E.-S., Kemp, J. P., Gregson, C. L., Evans, D. M., et al.** (2020). RSPO3  
780 impacts body fat distribution and regulates adipose cell biology in vitro. *Nat Commun*  
781 **11**, 2797.
- 782 **Longo, M., Zatterale, F., Naderi, J., Parrillo, L., Formisano, P., Raciti, G. A.,**  
783 **Beguilot, F. and Miele, C.** (2019). Adipose Tissue Dysfunction as Determinant of  
784 Obesity-Associated Metabolic Complications. *IJMS* **20**, 2358.

- 785 **Lumaquin, D., Johns, E., Weiss, J., Montal, E., Ooladipupo, O., Abuhashem, A.**  
786 **and White, R. M.** (2020). An *in vivo* reporter for tracking lipid droplet dynamics in  
787 transparent zebrafish. *bioRxiv* doi: 2020.11.09.375667.
- 788 **Malacrida, L. and Gratton, E.** (2018). LAURDAN fluorescence and phasor plots reveal  
789 the effects of a H<sub>2</sub>O<sub>2</sub> bolus in NIH-3T3 fibroblast membranes dynamics and hydration.  
790 *Free Radical Biology and Medicine* **128**, 144–156.
- 791 **Malacrida, L., Astrada, S., Briva, A., Bollati-Fogolín, M., Gratton, E. and Bagatolli,**  
792 **L. A.** (2016). Spectral phasor analysis of LAURDAN fluorescence in live A549 lung  
793 cells to study the hydration and time evolution of intracellular lamellar body-like  
794 structures. *Biochimica et Biophysica Acta (BBA) - Biomembranes* **1858**, 2625–2635.
- 795 **Malacrida, L., Jameson, D. M. and Gratton, E.** (2017). A multidimensional phasor  
796 approach reveals LAURDAN photophysics in NIH-3T3 cell membranes. *Sci Rep* **7**,  
797 9215.
- 798 **Maulucci, G., Di Giacinto, F., De Angelis, C., Cohen, O., Daniel, B., Ferreri, C., De**  
799 **Spirito, M. and Sasson, S.** (2018). Real time quantitative analysis of lipid storage and  
800 lipolysis pathways by confocal spectral imaging of intracellular micropolarity.  
801 *Biochimica et Biophysica Acta (BBA) - Molecular and Cell Biology of Lipids* **1863**, 783–  
802 793.
- 803 **Miehle, F., Möller, G., Cecil, A., Lintelmann, J., Wabitsch, M., Tokarz, J., Adamski,**  
804 **J. and Haid, M.** (2020). Lipidomic Phenotyping Reveals Extensive Lipid Remodeling  
805 during Adipogenesis in Human Adipocytes. *Metabolites* **10**, 217.
- 806 **Minchin, J. E. N. and Rawls, J. F.** (2017a). In vivo imaging and quantification of  
807 regional adiposity in zebrafish. In *Methods in Cell Biology*, pp. 3–27. Elsevier.
- 808 **Minchin, J. E. N. and Rawls, J. F.** (2017b). A classification system for zebrafish  
809 adipose tissues. *Disease Models & Mechanisms* **10**, 797–809.
- 810 **Minchin, J. E. N., Dahlman, I., Harvey, C. J., Mejhert, N., Singh, M. K., Epstein, J.**  
811 **A., Arner, P., Torres-Vázquez, J. and Rawls, J. F.** (2015). Plexin D1 determines body  
812 fat distribution by regulating the type V collagen microenvironment in visceral adipose  
813 tissue. *Proc Natl Acad Sci USA* **112**, 4363–4368.
- 814 **Olzmann, J. A. and Carvalho, P.** (2019). Dynamics and functions of lipid droplets.  
815 *Nature Reviews Molecular Cell Biology* **20**, 137–155.

- 816 **Parichy, D. M., Elizondo, M. R., Mills, M. G., Gordon, T. N. and Engeszer, R. E.**  
817 (2009). Normal table of postembryonic zebrafish development: Staging by externally  
818 visible anatomy of the living fish. *Developmental Dynamics* **238**, 2975–3015.
- 819 **Prentice, K. J., Saksi, J. and Hotamisligil, G. S.** (2019). Adipokine FABP4 integrates  
820 energy stores and counterregulatory metabolic responses. *Journal of Lipid Research*  
821 **60**, 734–740.
- 822 **Ranjit, S., Malacrida, L., Stakic, M. and Gratton, E.** (2019). Determination of the  
823 metabolic index using the fluorescence lifetime of free and bound nicotinamide adenine  
824 dinucleotide using the phasor approach. *J. Biophotonics* **12**, e201900156.
- 825 **Roberts, J. A., Miguel-Escalada, I., Slovik, K. J., Walsh, K. T., Hadzhiev, Y.,**  
826 **Sanges, R., Stupka, E., Marsh, E. K., Balciuniene, J., Balciunas, D., et al.** (2014).  
827 Targeted transgene integration overcomes variability of position effects in zebrafish.  
828 *Development* **141**, 715–724.
- 829 **Salmerón, C.** (2018). Adipogenesis in fish. *J Exp Biol* **221**, jeb161588.
- 830 **Sameni, S., Malacrida, L., Tan, Z. and Digman, M. A.** (2018). Alteration in Fluidity of  
831 Cell Plasma Membrane in Huntington Disease Revealed by Spectral Phasor Analysis.  
832 *Sci Rep* **8**, 734.
- 833 **Schindelin, J., Arganda-Carreras, I., Frise, E., Kaynig, V., Longair, M., Pietzsch,**  
834 **T., Preibisch, S., Rueden, C., Saalfeld, S., Schmid, B., et al.** (2012). Fiji: an open-  
835 source platform for biological-image analysis. *Nature Methods* **9**, 676–682.
- 836 **Schwalie, P. C., Dong, H., Zachara, M., Russeil, J., Alpern, D., Akchiche, N.,**  
837 **Caprara, C., Sun, W., Schlaudraff, K.-U., Soldati, G., et al.** (2018). A stromal cell  
838 population that inhibits adipogenesis in mammalian fat depots. *Nature* **559**, 103–108.
- 839 **Tang, Q. Q. and Lane, M. D.** (2012). Adipogenesis: From Stem Cell to Adipocyte.  
840 *Annual Review of Biochemistry* **81**, 715–736.
- 841 **Tang, W., Zeve, D., Suh, J. M., Bosnakovski, D., Kyba, M., Hammer, R. E.,**  
842 **Tallquist, M. D. and Graff, J. M.** (2008). White Fat Progenitor Cells Reside in the  
843 Adipose Vasculature. *Science* **322**, 583–586.
- 844 **Tontonoz, P., Graves, R. A., Lui, M., Hu, E., Tempst, P. and Spiegelman, B. M.**  
845 (1994). Adipocyte-specific transcription factor ARF6 is a heterodimeric complex of two  
846 nuclear hormone receptors, PPAR $\gamma$  and RXR $\alpha$ . *Nucleic Acids Research* **22**, 5628–  
847 5634.

- 848 **Vishvanath, L. and Gupta, R. K.** (2019). Contribution of adipogenesis to healthy  
849 adipose tissue expansion in obesity. *Journal of Clinical Investigation* **129**, 4022–4031.
- 850 **Wang, Y., Kaiser, M. S., Larson, J. D., Nasevicius, A., Clark, K. J., Wadman, S. A.,**  
851 **Roberg-Perez, S. E., Ekker, S. C., Hackett, P. B., McGrail, M., et al.** (2010). Moesin1  
852 and Ve-cadherin are required in endothelial cells during in vivo tubulogenesis.  
853 *Development* **137**, 3119–3128.
- 854 **Wang, H., Becuwe, M., Housden, B. E., Chitraju, C., Porras, A. J., Graham, M. M.,**  
855 **Liu, X. N., Thiam, A. R., Savage, D. B., Agarwal, A. K., et al.** (2016). Seipin is  
856 required for converting nascent to mature lipid droplets. *eLife* **5**, e16582.
- 857 **Warton, D. I., Wright, I. J., Falster, D. S. and Westoby, M.** (2006). Bivariate line-  
858 fitting methods for allometry. *Biol. Rev.* **81**, 259.
- 859 **Wilson, M. H., Ekker, S. C. and Farber, S. A.** (2021). Imaging cytoplasmic lipid  
860 droplets *in vivo* with fluorescent perilipin 2 and perilipin 3 knockin zebrafish. *bioRxiv*  
861 *doi: 2021.01.10.426109*.
- 862 **Zwick, R. K., Guerrero-Juarez, C. F., Horsley, V. and Plikus, M. V.** (2018).  
863 Anatomical, Physiological, and Functional Diversity of Adipose Tissue. *Cell Metabolism*  
864 **27**, 68–83.
- 865
- 866

867 **Figure legends**

868

869 **Figure 1. *fabp4a(-2.7):EGFPcaax* is expressed in early and mature adipocytes.**

870 **A.** The upper scheme shows the endogenous *fabp4a* gene in chromosome 19 with the  
871 transcription start site (TSS), exons (boxes), introns, and the coding sequence (CDS) in  
872 red. The cloned region is denoted between dashed lines. The lower scheme represents  
873 the vector used for transgenesis (tol2: tol2 sites; pA: SV40\_late\_polyA; cmlc2: cardiac  
874 myosin light chain 2 upstream region).

875 **B.** Epifluorescence microscopy images of live *fabp4a(-2.7):EGFPcaax* larvae from the  
876 incross of the F3 generation labelled with LipidTOX-Red. EGFP+ cells were present in  
877 the PVAT and AVAT depots. Asterisks indicate mature adipocytes stained with  
878 LipidTOX-Red with low (\*) or high EGFP expression (\*\*). Single arrows denote early  
879 adipocytes expressing EGFP with small lipid droplets. Double arrows indicate early  
880 adipocytes with EGFP expression without LipidTOX-Red staining. sb: swim bladder; g:  
881 gut. Scale bars: B: panoramic views: 200  $\mu$ m; insets: 50  $\mu$ m.

882

883 **Figure 2. Comparison of the expression pattern of *fabp4a(-2.7):EGFPcaxx* and**  
884 **endogenous *fabp4a* mRNA in larvae.**

885 Images of *fabp4a(-2.7):EGFPcaax* larvae of 21 dpf processed for WMISH,  
886 immunolabeled with anti-GFP and analyzed *in toto* through confocal microscopy.

887 **A.** Panoramic (upper row) and magnified image (lower row) of the abdominal region of  
888 a larvae labeled with *fabp4a* antisense probe. Yellow arrows denote the coincidence of  
889 EGFP (immunofluorescence) and WMISH signal. Arrows with asterisks show regions  
890 with WMISH labeling and no EGFP signal.

891 **B.** Images of the abdominal region of a larvae labeled with *fabp4a* sense probe. Yellow  
892 double arrows indicate regions with EGFP signal without WMISH labeling.

893 **C.** Images of the trunk of a larvae labeled with *fabp4a* antisense probe. Blue single  
894 arrows indicate pigment cells with EGFP signal. Blue double arrows show WMISH  
895 labeling in blood vessels.

896 Scale bars: A: 100  $\mu$ m (upper row), 50  $\mu$ m (lower row); B and C: 100  $\mu$ m.

897

898 **Figure 3. Distribution of labeled cells in the abdominal region of live *fabp4a(-***  
899 ***2.7):EGFPcaax* larvae of different stages.**

900 Larvae of the indicated stages were stained with LipidTOX-Red, mounted in agarose  
901 and imaged using confocal microscopy.

902 **A.** Transmitted light and 3D projection images of a larvae of SL 4.5mm (8 dpf). Yellow  
903 rectangles denote cells with transgene labeling. Insets A1 and A2 show confocal  
904 sections of these regions. Note membrane localization of EGFP and lack of LipidTOX-  
905 Red labeling. Cyan double arrows indicate pigment cells expressing the transgene.  
906 Cyan single arrows indicate pigments that scatter light.

907 **B.** 3D projection images of larvae of SL 5 mm (12 dpf). Yellow rectangles denote  
908 EGFP+ cells, magnified in B1 and B2. Cells with lipid droplets as well as without them  
909 (yellow arrows) can be seen in the same larvae in different positions.

910 **C.** 3D projection images of larvae of SL 6.3 mm (16 dpf) with initial PVAT depot  
911 formation. Note the presence of EGFP+ cells with unique cell-filling lipid droplets,  
912 irregular cells with several lipid droplets (yellow double arrows) and small cells without  
913 lipid droplets (yellow single arrows). Asterisks indicate cells without EGFP expression.

914 Scale bars: A: 100  $\mu\text{m}$  (panoramic view); 10  $\mu\text{m}$  (insets); B: 100  $\mu\text{m}$  (panoramic view);  
915 20  $\mu\text{m}$  (insets); C: 100  $\mu\text{m}$  (panoramic view); 20  $\mu\text{m}$  (insets).

916

917 **Figure 4. Interaction of early adipocytes with blood vessels.**

918 Live larvae from the cross of *fabp4a(-2.7):EGFPcaax* and *kdlr:mCherry* fish lines were  
919 imaged through confocal microscopy. Images presented here are 3D projections or  
920 single sections, as indicated.

921 **A.** Larvae of SL 6 mm (13 dpf) with many EGFP+ cells in its abdominal area, a few of  
922 them having lipid droplets (inset A1). Some of the cells are in contact with blood  
923 vessels (double arrows) and some of them are not (single arrows).

924 **B.** Larvae of SL 7 mm (16 dpf), with PVAT and AVAT depots (only some cells of each  
925 depot expresses EGFP). Insets B1, B2 and B3 show EGFP+ cells with lipid droplets in  
926 close apposition to blood vessels and in some cases surrounding them (B2). 3D  
927 projections and sections through the position indicated by the dashed line are shown.

928 Scale bars: A: 100  $\mu\text{m}$ ; B: 100  $\mu\text{m}$  (panoramic view), 20  $\mu\text{m}$  (insets).

929



930 **Figure 5. Different cell morphologies observed in *fabp4a(-2.7):EGFPcaax* larvae.**

931 **A.** *fabp4a(-2.7):EGFPcaax* larvae of 21 dpf were labeled with LipidTOX-Red and  
932 imaged *in vivo* through confocal microscopy. Images are 3D projections of confocal  
933 stacks, to show different cell morphologies found in these larvae.

934 **B.** Images of *fabp4a(-2.7):EGFPcaax; kdllr:mCherry* larvae of SL 8 (19 dpf). Note  
935 labeled cells in the AVAT depot with cytoplasmic projections which lay in close  
936 apposition to blood vessels. Images are 3D projections or sections as indicated.

937 **C.** High magnification confocal sections of EGFP+/LD- cells. Note the cytoplasmic  
938 inclusions observed in transmitted light.

939 Scale bars: A: 20  $\mu\text{m}$ ; B: 20  $\mu\text{m}$ ; C: 20  $\mu\text{m}$ .

940

941 **Figure 6. Larvae in different stages present cells with distinct lipid metabolic**  
942 **profiles.**

943 **A.** Representative hyperspectral images of adipocytes (“cell A” to “cell D”) in different  
944 stages of differentiation. Raw images are presented in gray and intensity based color  
945 scale. Images generated after phasor plot analysis make evident the EGFP and Nile  
946 Red profiles which are represented separately by different color scales. Scale bars: A:  
947 20  $\mu\text{m}$ .

948 **B.** Plot with the normalized distribution of the image pixels with respect to the fraction  
949 (expressed as percentage) of neutral lipids for each cell in (A).

950 **C.** Scatter plot showing the distribution range and center of mass of the cells analyzed  
951 in different larval stages. Both variables are expressed as the percentage of neutral  
952 lipids. The group of data coming from the same larval stage were enclosed by a  
953 manually generated convex hull shape just for visualization purposes. The dashed lines  
954 (DR=30; CM=60) generates the two regions considered in (D) and (E). The numbers in  
955 brackets indicate the total number of larvae and the total number of cells analyzed in  
956 each stage.

957 **D.** Data within (DR<30 / CM<60) and outside (DR>30 / CM>60) the region considered  
958 in (C) were separated and compared. For center of mass: (\*)  $p=2.06 \times 10^{-13}$  for median  
959 comparison (Mann-Whitney test),  $p=1.62 \times 10^{-4}$  for coefficient of variation comparison  
960 (Fligner-Killeen test); (\*\*)  $p=2.24 \times 10^{-16}$  for median comparison (Mann-Whitney test),  
961  $p=7.1 \times 10^{-6}$  (Fligner-Killeen test).

962 **E.** Representation of the percentage of cells in each group (DR<30 / CM<60 and  
963 DR>30 / CM>60) with respect to the larval stage presented in days post-fertilization  
964 (dpf).

965 **F.** Representation of the distribution range (as the size of the dots) and center of mass  
966 for the cells within some of the larva analyzed; each larva had a different standard  
967 length.

968

Figure 1

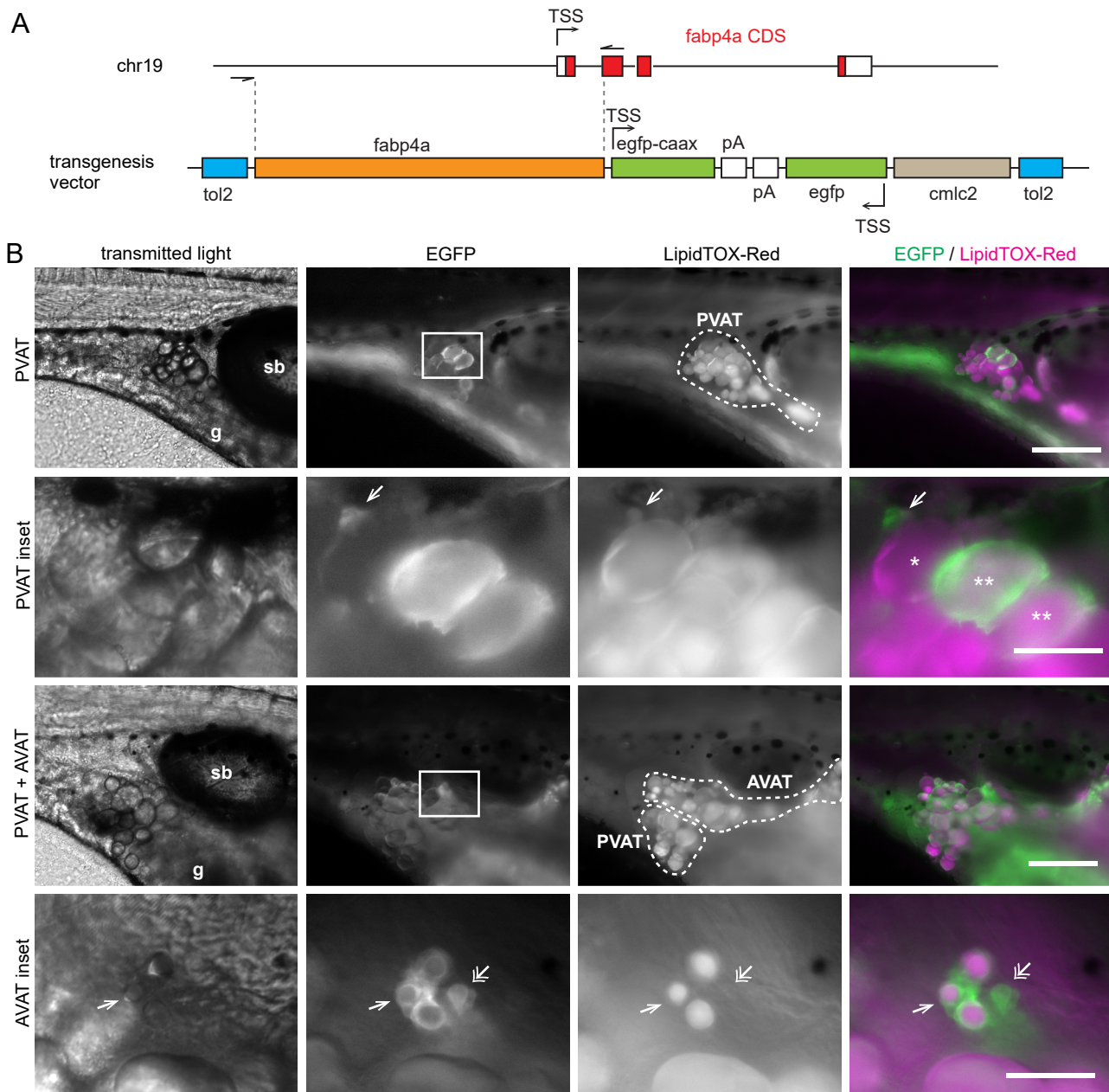


Figure 2

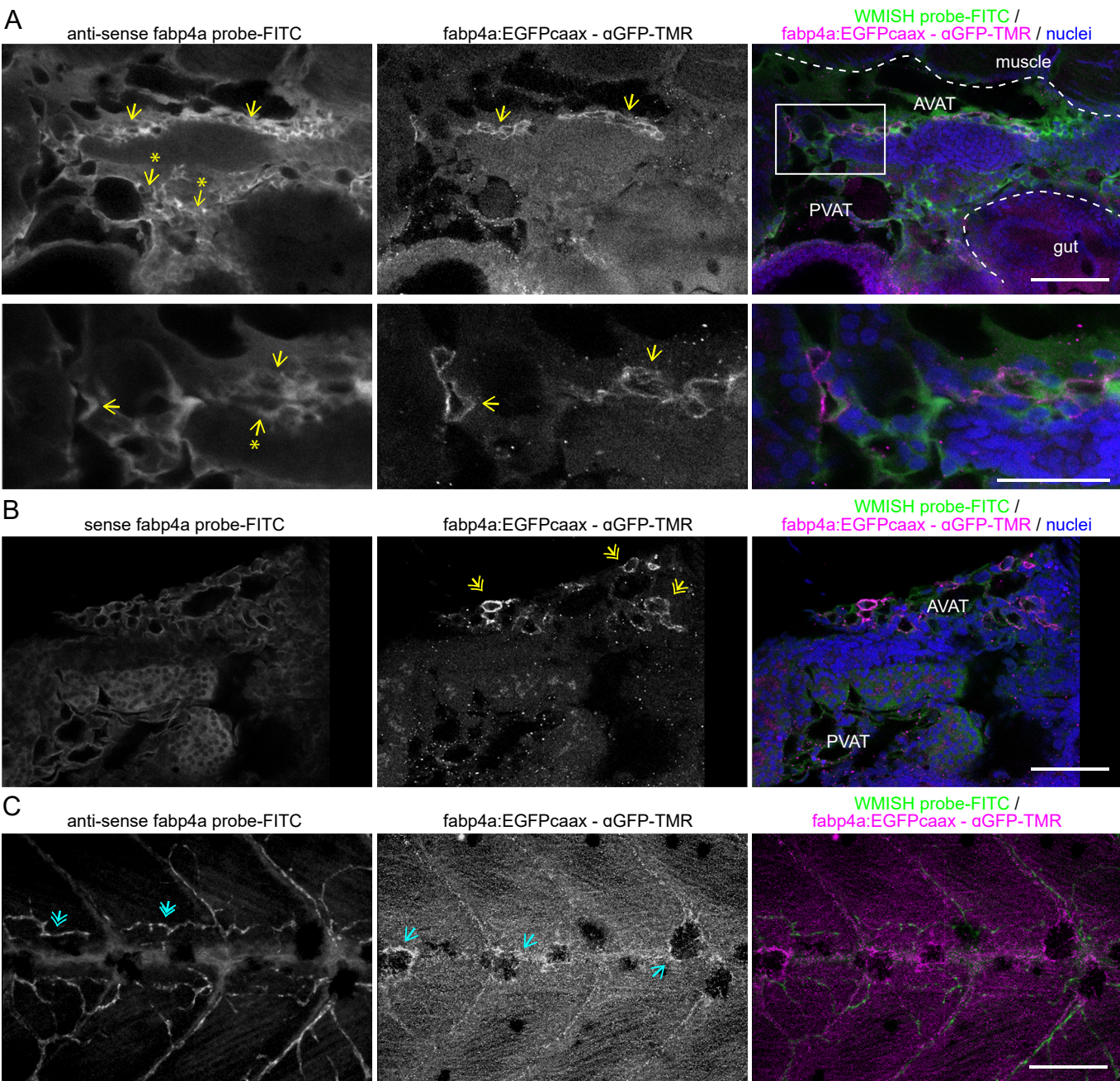
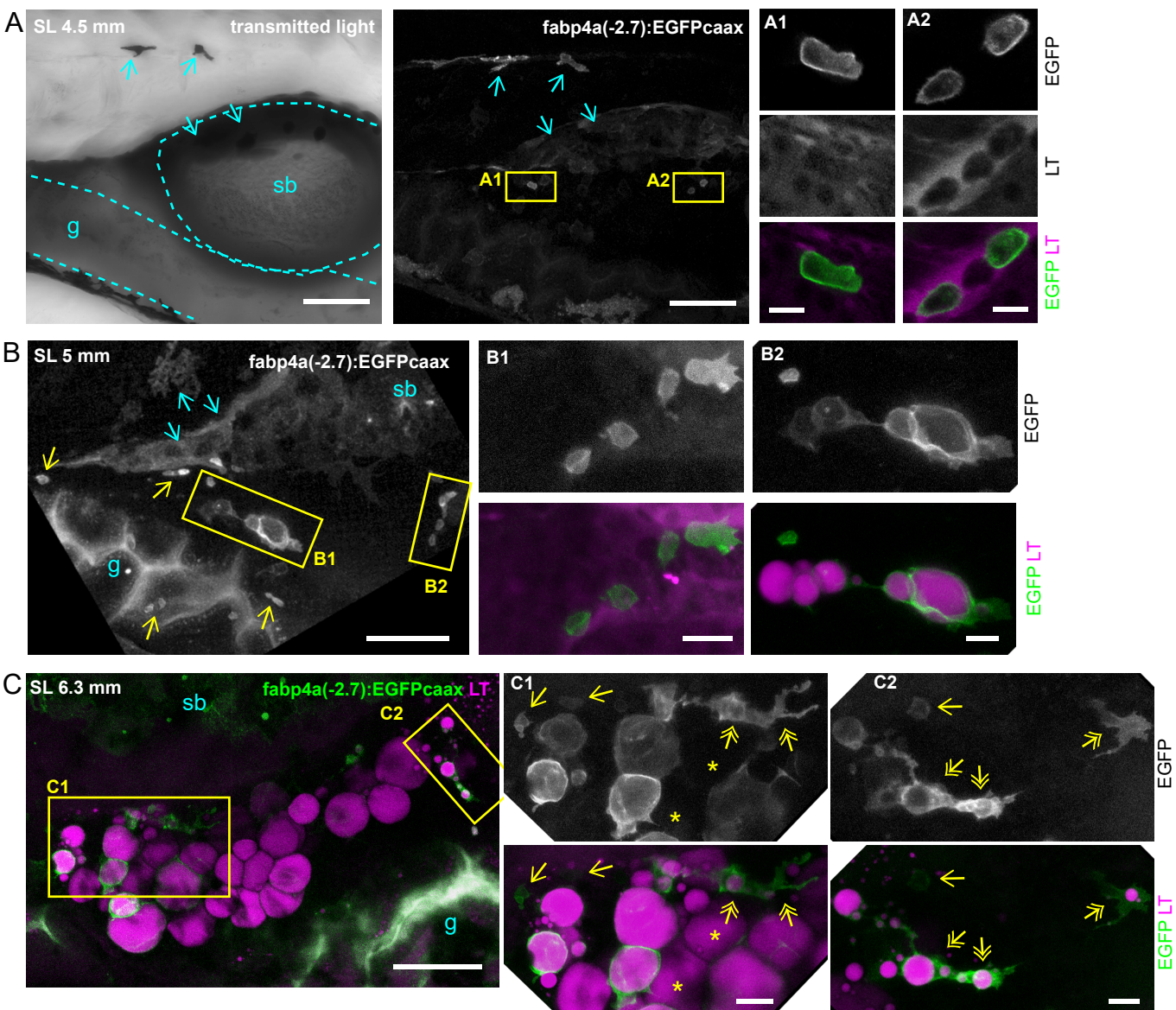


Figure 3



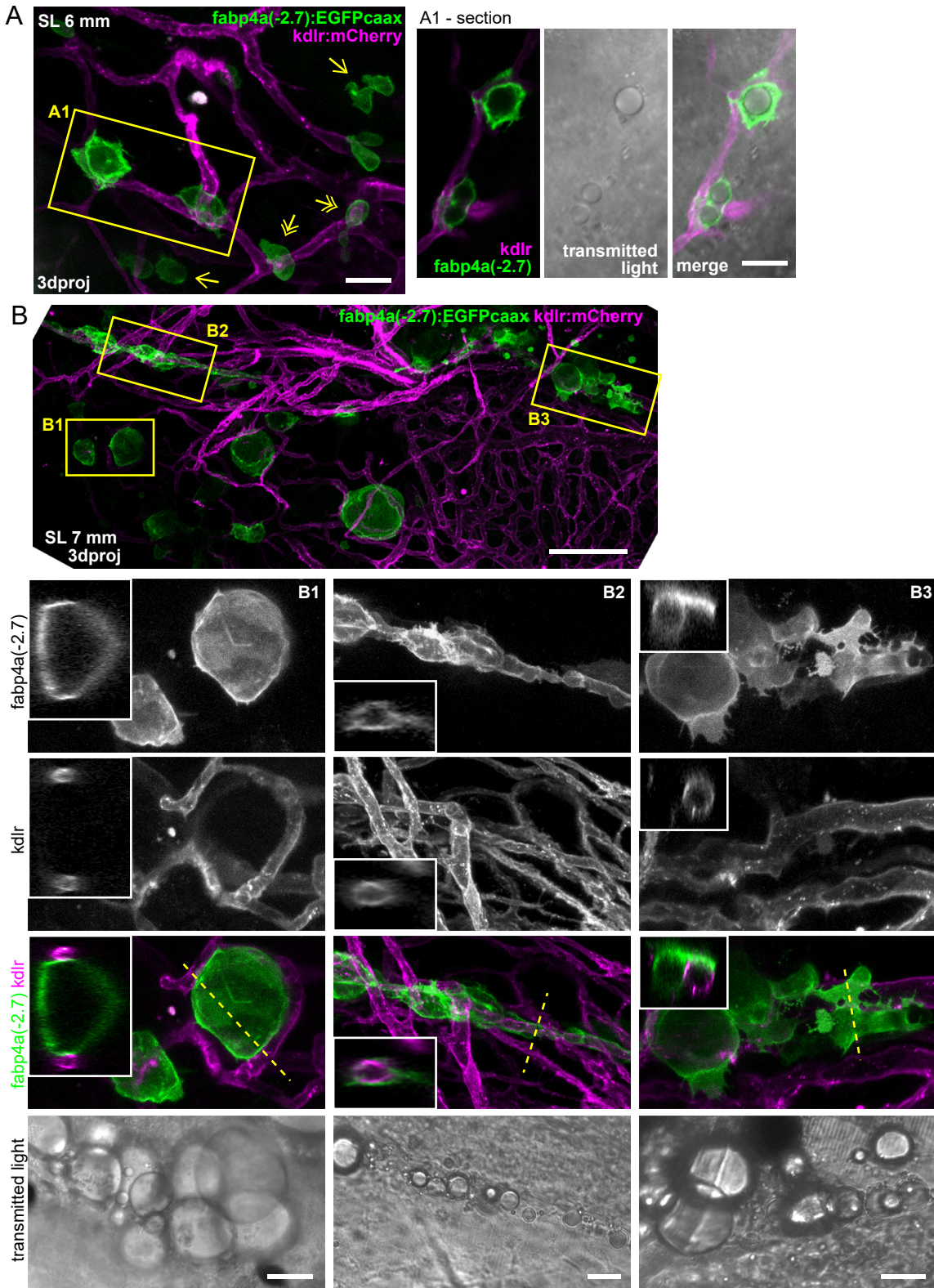


Figure 5

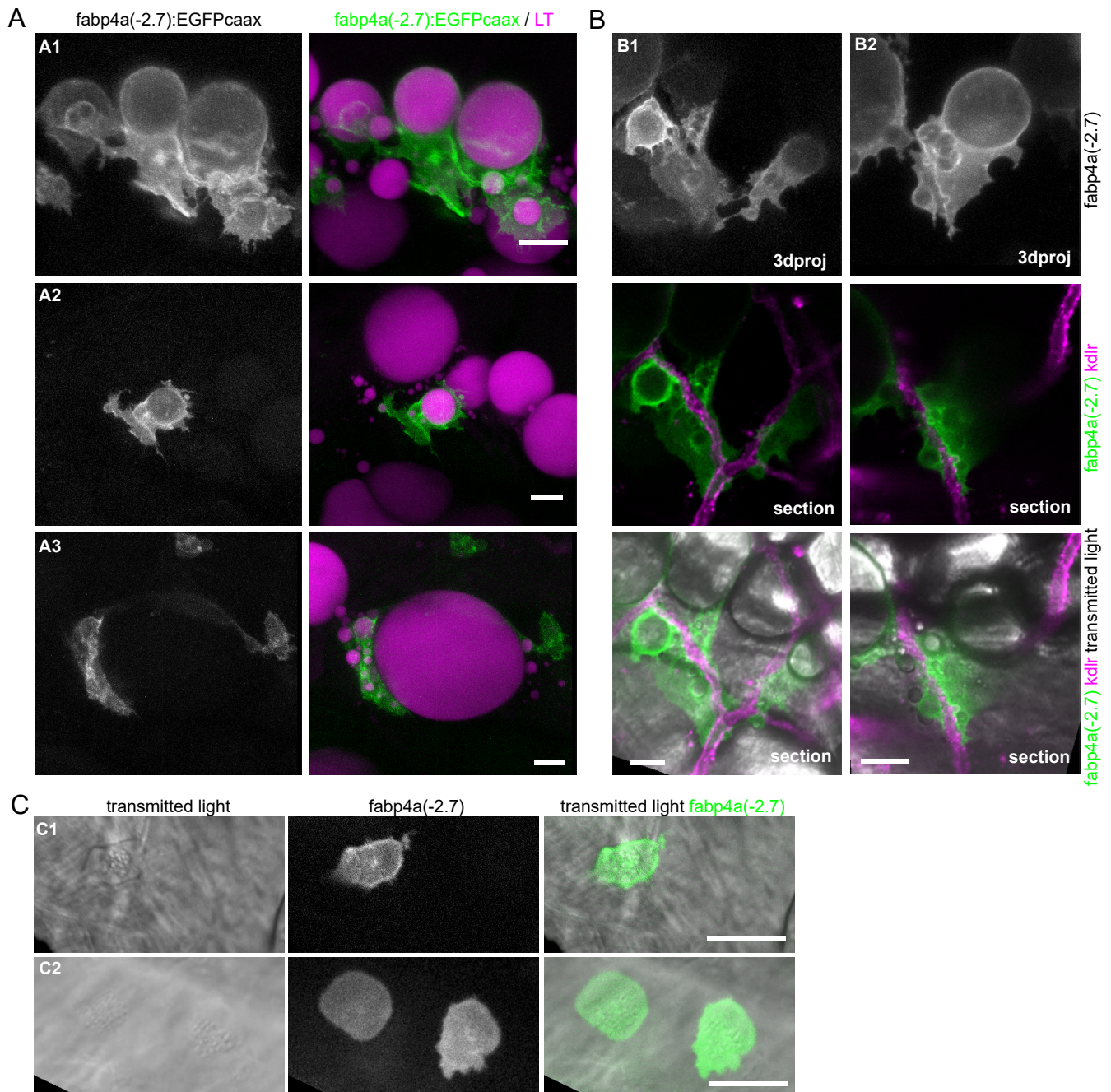
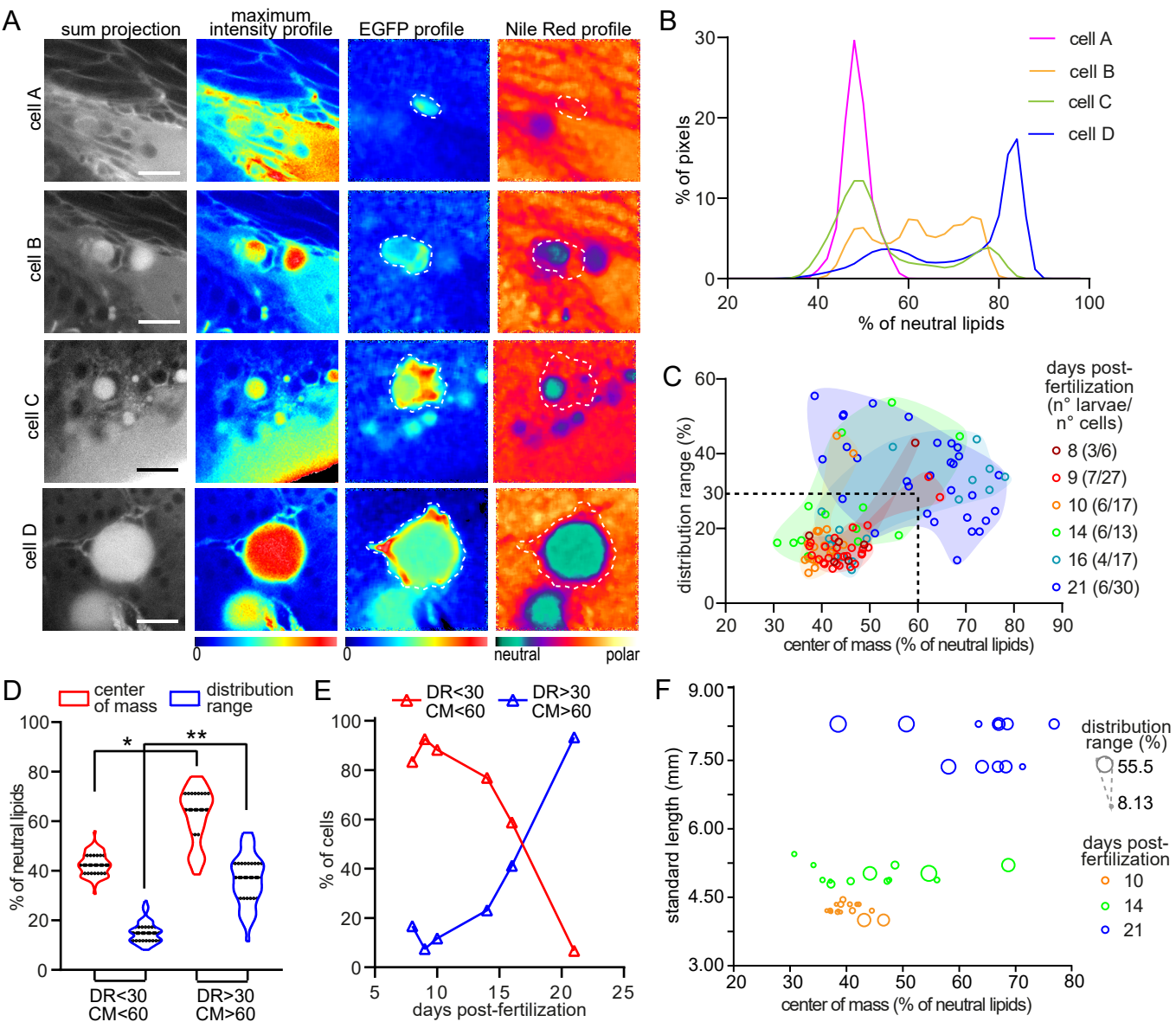
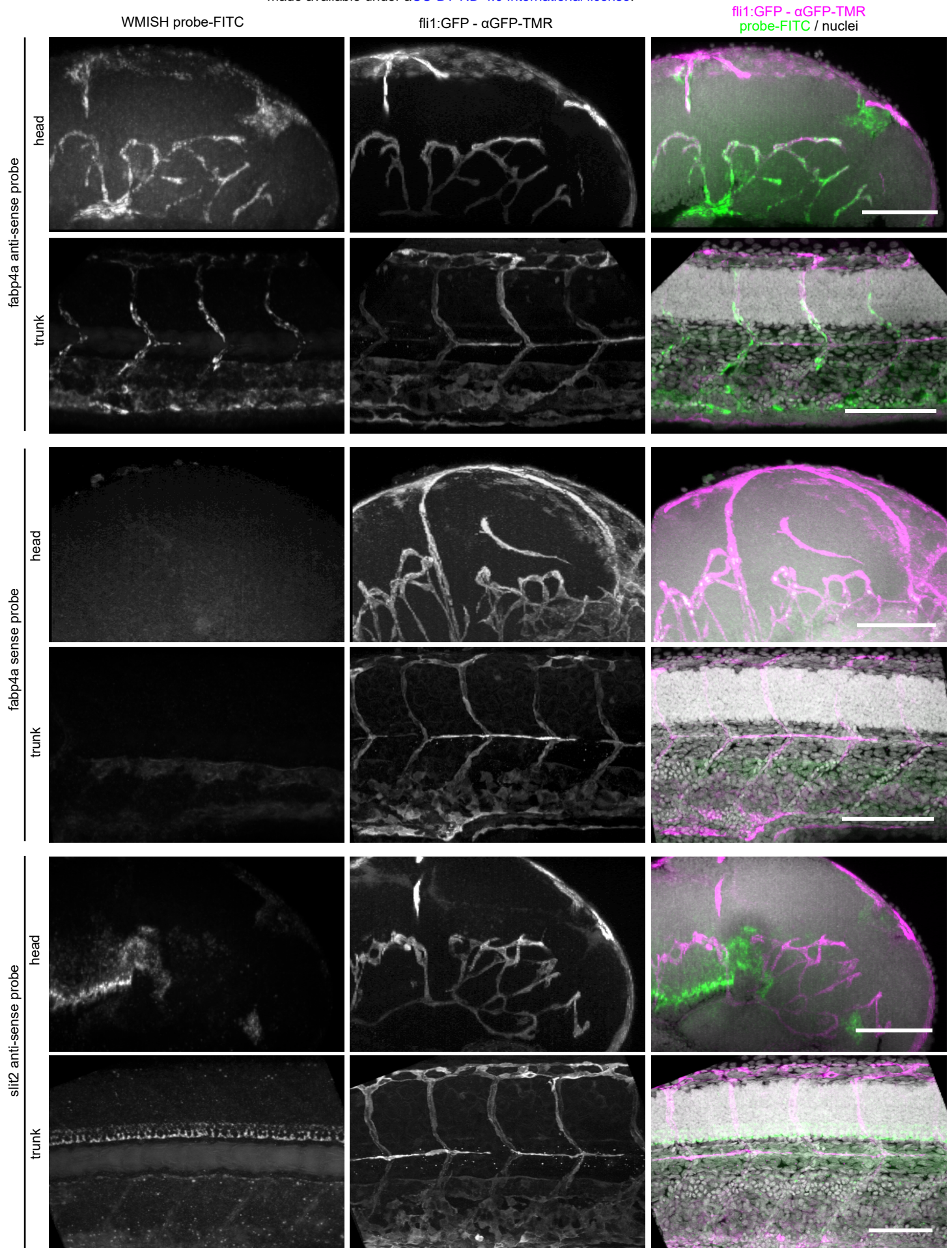


Figure 6





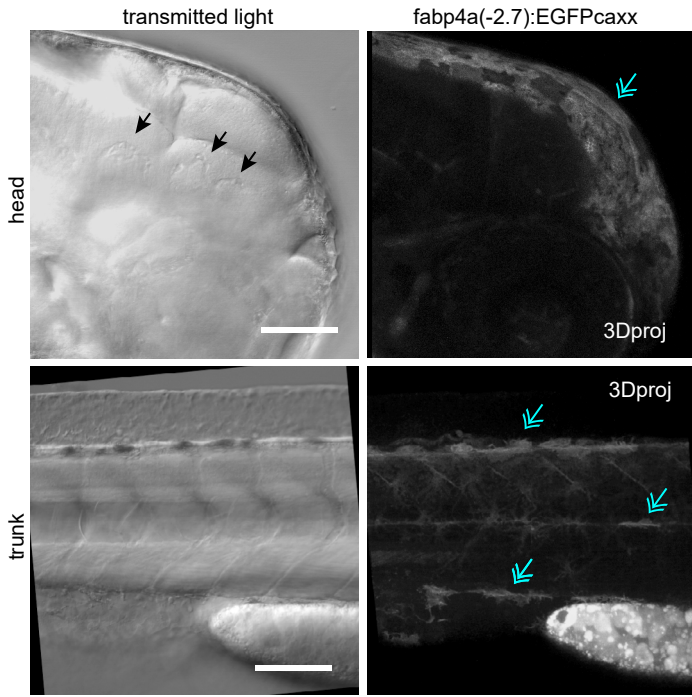


969 **Figure S1. Set up of MWISH and immunofluorescence in embryos.**

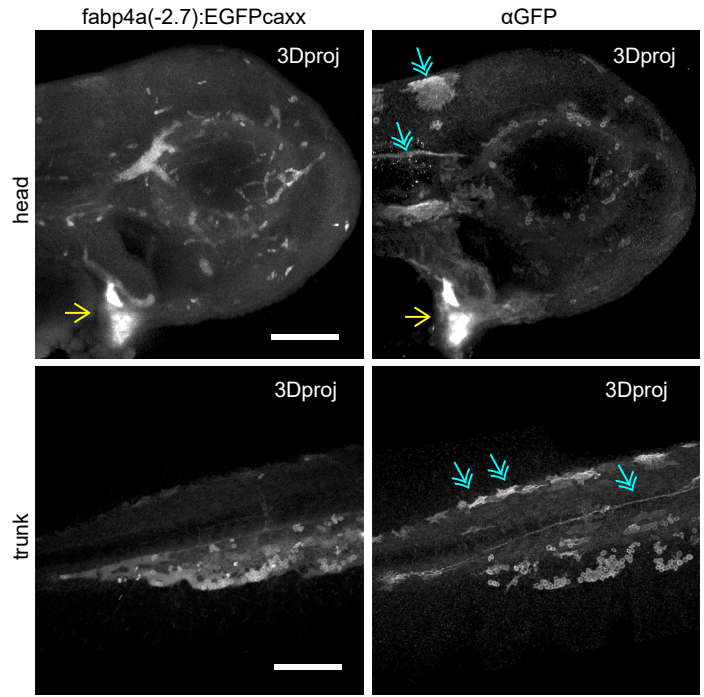
970 Images of 2 dpf *fli1:EGFP* embryos. WMISH was performed with antisense and sense  
971 probes against *fabp4a*, and with previously validated antisense probes for *slit2*. After  
972 immunolabeling with anti-GFP, embryos were imaged *in toto* through confocal  
973 microscopy. 3D projections generated from confocal stacks are shown. Scale bars: 100  
974  $\mu\text{m}$ .

975

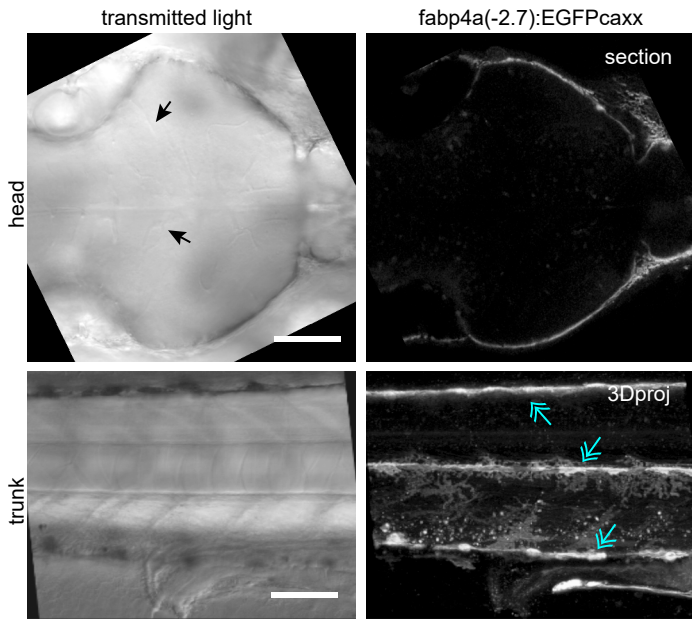
**A** live 2 dpf embryos



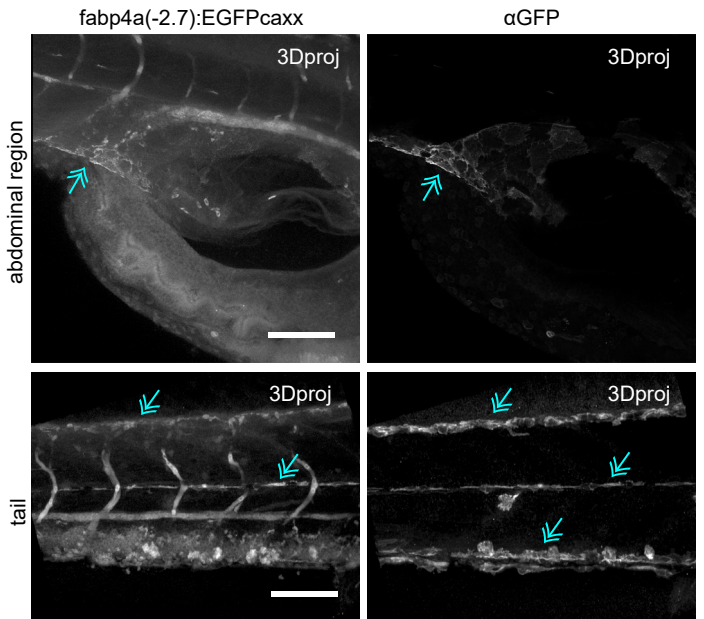
**B** 2 dpf - whole mount immunofluorescence



**C** live 5 dpf embryos



**D** 5 dpf - whole mount immunofluorescence

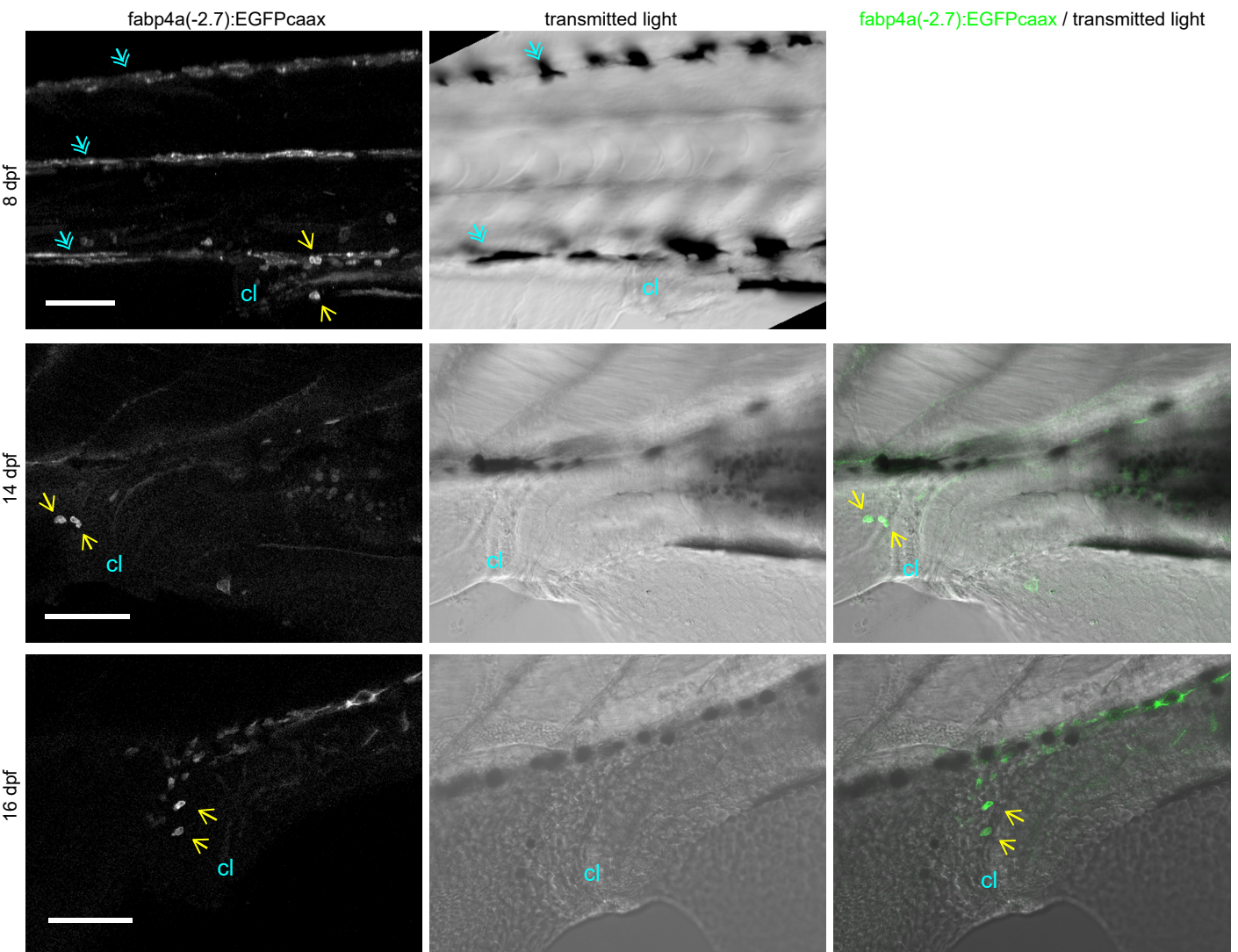


976 **Figure S2. Expression domains of *fabp4a(-2.7):EGFPcaax* in embryos.**

977 **A and C.** Images of live embryos of 2 and 5 dpf. Transmitted light or fluorescence  
978 images were acquired through confocal microscopy and presented either as single  
979 sections or 3D projections (3Dproj). In transmitted light it is possible to observe blood  
980 vessels (black arrows) and the lack of fluorescence colocalization.

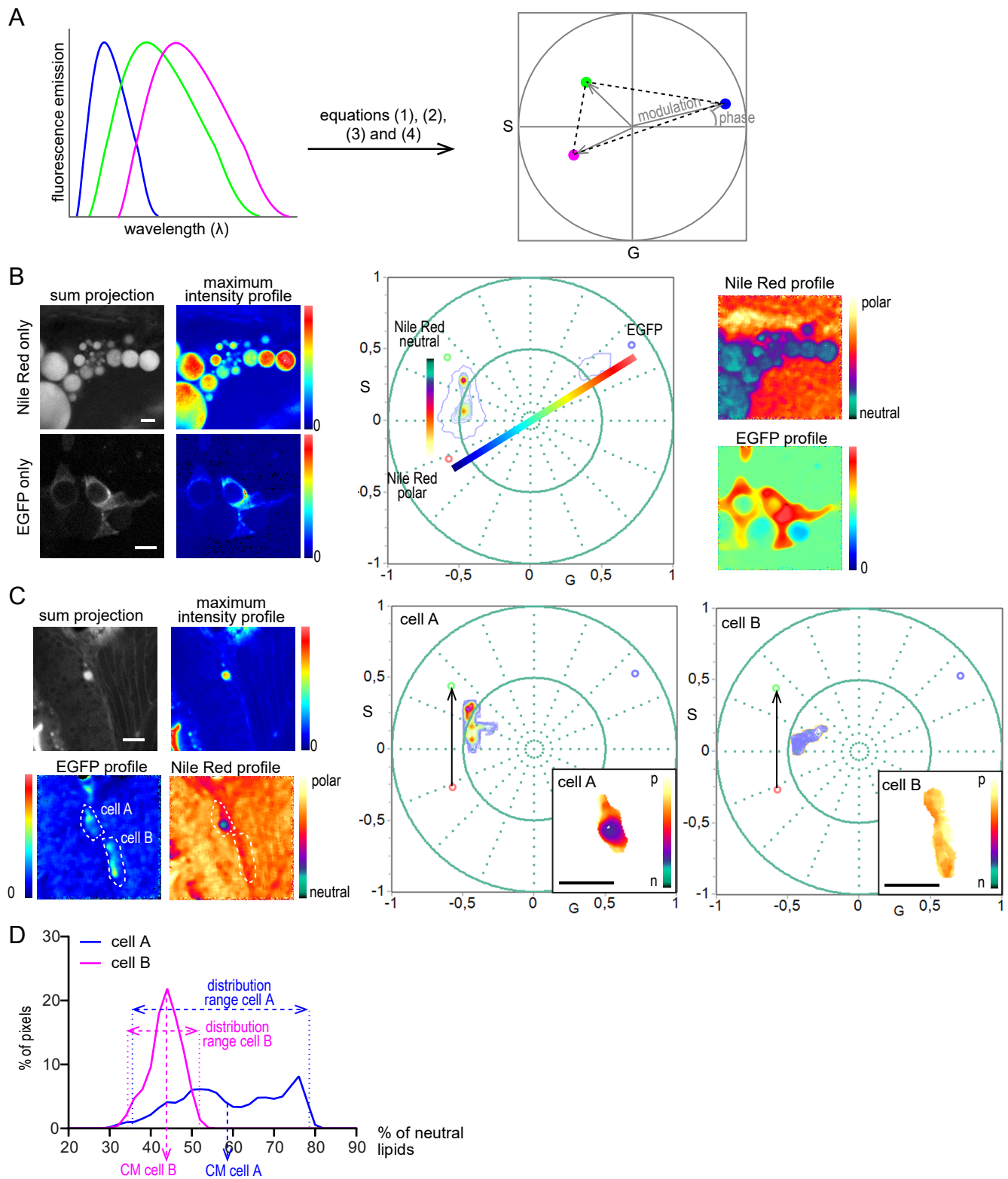
981 **B and D.** Images of fixed embryos of 2 and 5 dpf immunostained with anti-GFP  
982 antibody. Both endogenous GFP and immunolabeling signals are shown. Yellow  
983 arrows show the positive immunolabeling signal in heart cells. Blue-double arrows  
984 indicate the presence of fluorescence in pigment cells, both in live and fixed embryos,  
985 as well as through immunolabeling.

986 Scale bars: A-D: 100  $\mu$ m.



987 **Figure S3. *fabp4a(-2.7):EGFPcaax* expressing cells in the tail region of larvae at**  
988 **different stages.** Images of live larvae analyzed through confocal microscopy at  
989 different stages (expressed as dpf). EGFP+/LD- cells were present in all stages  
990 analyzed, including in the cloaca region (yellow arrows). The fluorescence image of 8  
991 dpf larvae is a 3D projection to note the presence of labeled pigmentary cells (cyan  
992 double arrows). cl: cloaca. Scale bars: 100  $\mu$ m.

Figure S4



993 **Figure S4. Analysis of the lipid metabolic profile of EGFP+ cells.**

994 **A.** Schematic representation of the transformation of the individual spectra of three  
995 different fluorophores into the same phasor plot using equations (1) to (4) indicated in  
996 “Materials and Methods” section. Dashed lines indicate the area (triangle) in the phasor  
997 plot in which pixels with the combination of the three different fluorophores will appear.

998 **B.** Examples of hyperspectral images of control cells and the localization of each pixel  
999 in a phasor plot. Images in the left are projections of spectral images and were colored  
1000 according to pixel intensity maximum. Images of wild type larvae stained with Nile Red  
1001 (“Nile Red only”) lay within a line-shaped trajectory, corresponding to regions of  
1002 different lipid polarity within the cell, were used to define the position of two of the  
1003 components (Nile Red in a polar environment: red circle; Nile Red in a neutral  
1004 environment: green circle). Instead, images of cells in *fabp4a(-2.7):EGFPcaax* larvae  
1005 without staining (“EGFP only”) appear in a defined region with low phase angle, which  
1006 was used to define the position of the third component (EGFP: blue circle). The images  
1007 in the right were colored according to the position of pixels in the phasor plot (the color  
1008 scales were superimposed to the Nile Red trajectory and the EGFP axis for improving  
1009 clarity).

1010 **C.** Example of cells in a *fabp4a(-2.7):EGFPcaax* larvae of 8 dpf stained with Nile Red.  
1011 Images were colored according to pixel intensity or to the position of pixels in the  
1012 phasor. Phasor plots corresponding to the thresholded cells are presented in the right  
1013 side. The direction of the Nile Red axis used for plots in (D) is denoted by a black  
1014 arrow.

1015 **D.** Normalized distribution of pixels along the Nile Red axis in the phasor plot for the  
1016 cells in (C). The “Nile Red axis” corresponds to the percentage of polar lipids in the  
1017 region of the cell analyzed. The center of mass and range of these distributions were  
1018 calculated as described in the “Material and methods” section and are schematically  
1019 represented in the plot. Scale bars: B: 20  $\mu\text{m}$ ; C: 50  $\mu\text{m}$ .

1020



1021 **Movie 1.** Time-lapse imaging of EGFP+/LD- cells. The membrane EGFP signal is in  
1022 green and the transmitted light in grey. Time is showed in minutes:seconds format.  
1023 Scale bar: 10  $\mu\text{m}$